

Journal Pre-proof

Geochemistry, detrital zircon geochronology and Hf isotope of the clastic rocks in southern Tibet: implications for the Jurassic-Cretaceous tectonic evolution of the Lhasa terrane

Youqing Wei, Zhidan Zhao, Yaoling Niu, Di-Cheng Zhu, Donald J. DePaolo, Tianjing Jing, Dong Liu, Qi Guan, Lawangin Sheikh

PII: S1342-937X(19)30265-5

DOI: <https://doi.org/10.1016/j.gr.2019.08.014>

Reference: GR 2215

To appear in: *Gondwana Research*

Received Date: 30 May 2019

Revised Date: 20 August 2019

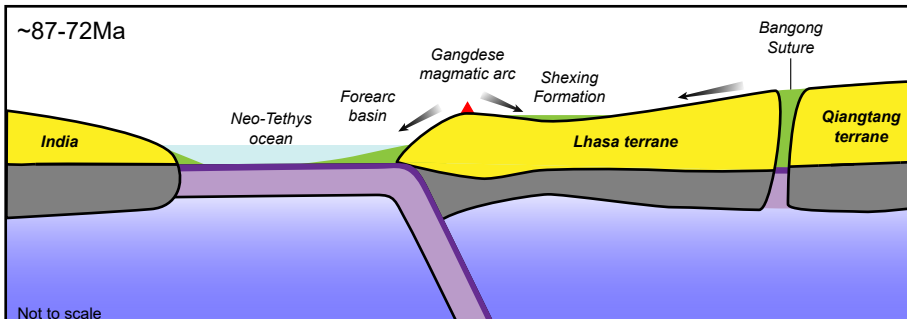
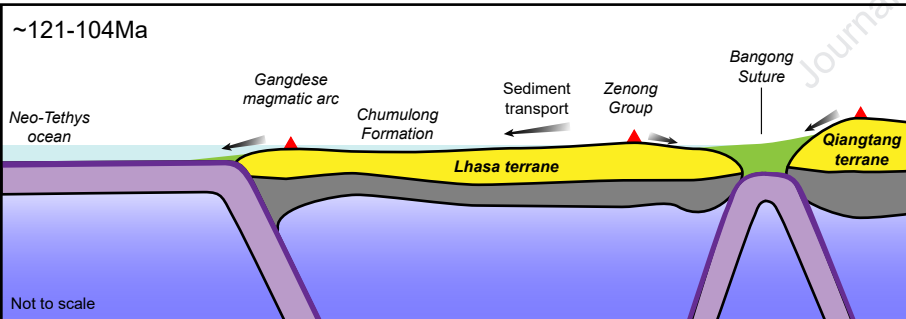
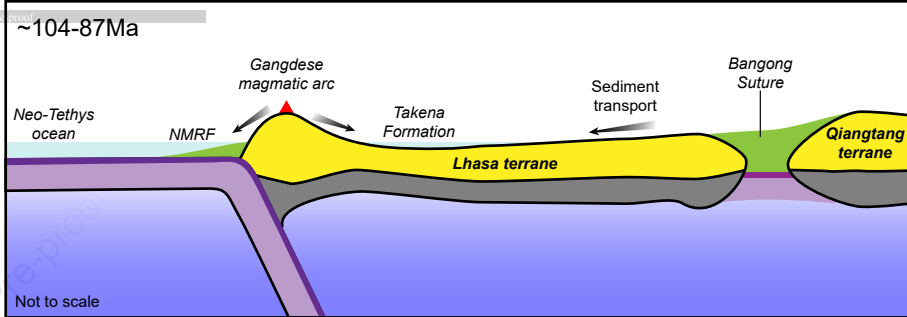
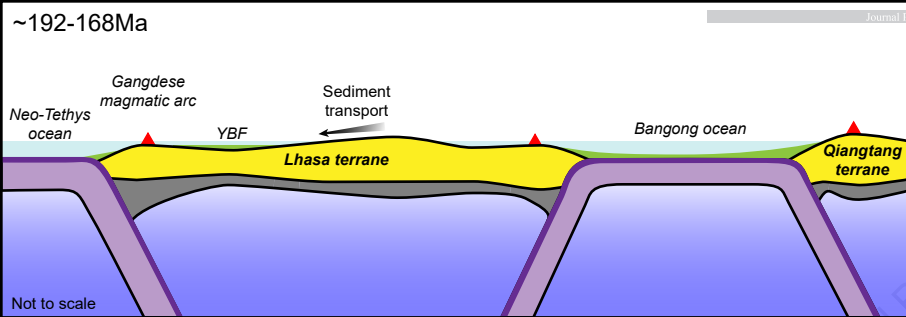
Accepted Date: 25 August 2019

Please cite this article as: Wei, Y., Zhao, Z., Niu, Y., Zhu, D.-C., DePaolo, D.J., Jing, T., Liu, D., Guan, Q., Sheikh, L., Geochemistry, detrital zircon geochronology and Hf isotope of the clastic rocks in southern Tibet: implications for the Jurassic-Cretaceous tectonic evolution of the Lhasa terrane, *Gondwana Research*, <https://doi.org/10.1016/j.gr.2019.08.014>.

This is a PDF file of an article that has undergone enhancements after acceptance, such as the addition of a cover page and metadata, and formatting for readability, but it is not yet the definitive version of record. This version will undergo additional copyediting, typesetting and review before it is published in its final form, but we are providing this version to give early visibility of the article. Please note that, during the production process, errors may be discovered which could affect the content, and all legal disclaimers that apply to the journal pertain.

© 2019 International Association for Gondwana Research. Published by Elsevier B.V. All rights reserved.





1 **Geochemistry, detrital zircon geochronology and Hf isotope of**
2 **the clastic rocks in southern Tibet: implications for the**
3 **Jurassic-Cretaceous tectonic evolution of the Lhasa terrane**

4 Youqing Wei^{a,b,d}, Zhidan Zhao^{c,*}, Yaoling Niu^{a,c,d,e}, Di-Cheng Zhu^c, Donald J. DePaolo^f,
5 Tianjing Jing^c, Dong Liu^c, Qi Guan^g, and Lawangin Sheikh^c

6

7 ^aInstitute of Oceanology, Chinese Academy of Sciences, Qingdao 266071, China

8 ^bShandong Provincial Key Laboratory of Depositional Mineralization & Sedimentary
9 Mineral, Shandong University of Science and Technology

10 ^cState Key Laboratory of Geological Processes and Mineral Resources, and School of
11 Earth Science and Resources, China University of Geosciences, Beijing 100083,
12 China

13 ^dLaboratory for Marine Geology, Qingdao National Laboratory for Marine Science
14 and Technology, Qingdao 266061, China

15 ^eDepartment of Earth Sciences, Durham University, Durham HD1 3LE, UK

16 ^fDepartment of Earth and Planetary Sciences, University of California, Berkeley, CA
17 94720

18 ^gHebei GEO University, Shijiazhuang 050031, China

19

20 *Corresponding author at:

21 State Key Laboratory of Geological Processes and Mineral Resources, and School of

22 Earth Science and Resources, China University of Geosciences, Beijing 100083, China.

23 Tel: +86-10-82321115

24 E-mail: zdzhao@cugb.edu.cn

25 **Abstract**

26 In order to reconstruct tectonic evolution history of the southern margin of Asia
27 (i.e., Lhasa terrane) before the India-Asia collision, here we present a comprehensive
28 study on the clastic rocks in the southern Lhasa terrane with new perspectives from
29 sedimentary geochemistry, detrital zircon geochronology and Hf isotope. Clasts from
30 the Jurassic-Early Cretaceous sedimentary sequences (i.e., Yeba and Chumulong
31 Formations) display high compositional maturity and experienced moderate to high
32 degree of chemical weathering, whereas those from the late Early-Late Cretaceous
33 sequences (Ngamring and Shexing Formations) are characterized by low
34 compositional maturity with insignificant chemical weathering. Our results lead to a
35 coherent scenario for the evolution history of the Lhasa terrane. During the
36 Early-Middle Jurassic (~192-168Ma), the Lhasa terrane was speculated to be an
37 isolated geological block. The Yeba Formation is best understood as being deposited
38 in a back-arc basin induced by northward subduction of the Neo-Tethys ocean with
39 sediments coming from the interiors of the Lhasa terrane. The Middle Jurassic-Early
40 Cretaceous Lhasa-Qiangtang collision resulted in the formation of a composite
41 foreland basin with southward-flowing rivers carrying clastic materials from the

42 uplifted northern Lhasa and/or Qiangtang terranes. During the late Early-Late
43 Cretaceous (~104-72Ma), the Gangdese magmatic arc was uplifted rapidly above the
44 sea level, forming turbidites (Ngamring Formation) in the Xigaze forearc basin and
45 fluvial red beds (Shexing Formation) on the retro-arc side. At the end of Late
46 Cretaceous, the Lhasa terrane was likely to have been uplifted to high elevation
47 forming an Andean-type margin resembling the modern South America before the
48 India-Asia collision.

49 **Keyword:** geochemistry; detrital zircon geochronology; Hf isotope; Lhasa terrane;
50 southern Tibet

51 **1 Introduction**

52 The theory of plate tectonics explains the way how physiographic features of the
53 Earth are shaped and evolve over time. Serving as an archetype of continent-continent
54 collision, the Tibetan Plateau is thought to have influenced global climate and
55 seawater chemistry (Molnar et al., 2010; Richter et al., 1992). It is widely accepted
56 that the Tibetan Plateau is a Cenozoic feature resulting from the India-Asia collision
57 and subsequent subduction of the Indian lithosphere beneath Asia (e.g., Chung et al.,
58 1998; Harrison et al., 1992). However, recent investigations have proposed that the
59 southernmost portion of Asia (i.e., the Lhasa terrane) might have attained high
60 elevation immediately before the collision (Kapp et al., 2005, 2007; Leier et al., 2007a;
61 Murphy et al., 1997; Zhu et al., 2017). It is crucial to ascertain the pre-collisional

62 tectonic evolution history of the Lhasa terrane for better understanding the mechanism
63 and time-scale of the plateau formation.

64 Chemical composition holds important information on the provenance of clastic
65 sedimentary rocks. Compared with petrographic method, the geochemical approach
66 has been shown to be more effective in studying matrix-rich sandstones and shales,
67 and in some cases can be used to quantify the occurrence and/or extent of sedimentary
68 processes such as weathering, sorting and diagenesis (McLennan et al., 1993).
69 Previous studies have correlated chemical weathering intensity of clastic rocks with
70 climate and relief of the source terranes (e.g., Fedo et al., 1997; Nesbitt and Young,
71 1982; Yan et al., 2010). Sediments having undergone significant chemical weathering
72 are likely to be deposited in low-relief regions with warm and humid climate (e.g.,
73 sediments of the Congo Rivers; Wronkiewicz and Condie, 1987), whereas those less
74 affected by chemical weathering are supposed to be derived from high-relief regions
75 with cold and arid climate (e.g., Pleistocene glacial clays and tillites; Nesbitt and
76 Young, 1996). Existing paleomagnetic data show that the southern margin of the
77 Lhasa terrane was close to the equator in the time span from the Early Jurassic ($\sim 3.7^\circ$
78 S; Li et al., 2016) to Late Cretaceous ($\sim 15^\circ$ N; Sun et al., 2012). In this case, climate
79 change of the Lhasa terrane is largely related to tectonism-induced regional uplift,
80 which can be best addressed using sedimentary geochemical approaches.

81 During chemical weathering, unstable components (including volcanic fragments,
82 ferromagnesian minerals and feldspars) are largely decomposed but zircon survives

83 and is enriched in the sediments due to its physiochemical resistance. This makes
84 zircon a powerful tracer for studying provenances of terrigenous sedimentary rocks
85 (e.g., Wu et al., 2010; Zhu et al., 2011b). As potential provenance, the magmatic rocks
86 emplaced in the southern Lhasa terrane and some localities in the northern Lhasa
87 terrane have zircons with positive $\epsilon\text{Hf}(t)$, whereas rocks from the central Lhasa
88 terrane have negative $\epsilon\text{Hf}(t)$ (Hou et al., 2015; Zhu et al., 2011a). Moreover, detrital
89 zircons from the pre-Mesozoic rocks in the Lhasa terrane have a distinctive age
90 cluster of $\sim 1170\text{Ma}$, whereas those from the western Qiangtang and Tethyan
91 Himalaya terranes define an age peak of $\sim 950\text{Ma}$ (Zhu et al., 2011b). The differences
92 in detrital zircon age distribution and Hf isotopic composition serve as a unique tool
93 for interpreting tectonic evolution history of the Lhasa terrane recorded in
94 sedimentary rocks.

95 In this paper, we present the results of our study using a such combined approach,
96 including bulk-rock geochemistry, detrital zircon U-Pb geochronology and Hf isotope
97 on different types of clastic rocks (sandstones and mudstones) from the southern
98 Lhasa terrane. Although previous studies have proposed numerous tectonic models for
99 the Mesozoic Lhasa terrane based on magmatism (e.g., Hou et al., 2015; Zhu et al.,
100 2011), tectonism (Yin and Harrison, 2000; Murphy et al., 1997) or stratigraphy (Kapp
101 et al., 2005; Leier et al., 2007a), this paper is unique to provide new constraints on the
102 changes of paleoclimate and sedimentary provenance through time. With these data,
103 we are able to reconstruct the evolution history of the Lhasa terrane prior to the

104 India-Asia collision.

105 **2 Geological background and sampling**

106 **2.1 Geological setting**

107 The Tibetan Plateau comprises a series of allochthonous Gondwanan continental
108 fragments that were accreted to Asia since the Early Paleozoic (Yin and Harrison,
109 2000; Zhu et al., 2013). These fragments are, from north to south, Songpan-Ganzi
110 flysch complex, Qiangtang terrane, Lhasa terrane and the Himalayas, separated by
111 Jinsha, Bangong and Indus-Yarlung Zangbo Sutures (Fig. 1A). Serving as the
112 southernmost tectonic unit of Asia, the Lhasa terrane is an E-W trending geological
113 block that can be divided into the northern, central and southern subterrane due to
114 different magmatism and sedimentary covers (Hou et al., 2015; Zhu et al., 2011a).
115 The ancient metamorphic basement of the Lhasa terrane is represented by the
116 Nyainqentanglha Group in the central Lhasa terrane, which is covered with
117 widespread Permian-Carboniferous metasedimentary strata (Zhu et al., 2011a, 2013).
118 The northern Lhasa terrane has extensive Cretaceous strata and minor
119 Triassic-Jurassic strata (Kapp et al., 2005, 2007; Zhu et al., 2011a). The southern
120 margin of Lhasa terrane is represented by the Gangdese magmatic arc (GMA, Fig. 1A;
121 also named as Gangdese batholith for the plutonic equivalents because of significant
122 erosion), from which volcanism since the Middle Triassic has been well documented
123 (e.g., Liu et al., 2018; Mo et al., 2008; Wang et al., 2016; Wei et al., 2017; Zhu et al.,

124 2008, 2011a). In the southern Lhasa terrane, sedimentary strata predominantly of
125 Jurassic-Cretaceous age are well preserved (Zhu et al., 2013) and mainly comprise
126 Lower-Middle Jurassic back-arc sequence of the Yeba Formation (Liu et al., 2018;
127 Wei et al., 2017; Zhu et al., 2008) , Lower Cretaceous fluvial and marginal marine
128 clastic successions of the Linbuzong and Chumulong Formations (Leier et al., 2007a),
129 Upper Cretaceous shallow-marine deposits of the Takena Formation (Leier et al.,
130 2007b) and fluvial red beds of the Shexing Formation (Sun et al., 2012) . There are
131 also small-scale and scattered exposures of Upper Jurassic limestones of the
132 Duodigou Formation showing fault contact with the underlying Yeba Formation. To
133 the south of the Gangdese magmatic arc, a Cretaceous-Paleogene forearc succession
134 was identified, i.e., Xigaze forearc basin (An et al., 2014; Wang et al., 2012; Wu et al.,
135 2010). The Xigaze forearc succession is subdivided into the Chongdui, Sangzugang,
136 Ngamring, Padana and Qubeiya Formations from the bottom to the top (Hu et al.,
137 2016). Representing the main turbiditic fill of the Xigaze forearc basin, the Ngamring
138 Formation displays conformable contact with underlying deep-water sediments of the
139 Chongdui Formation and the overlying Padana Formation, and locally in fault contact
140 with the Xigaze ophiolite in the south (An et al., 2014).

141 **2.2 Sampling**

142 **2.2.1 Yeba Formation**

143 Extending E-W trending for ~250km in the eastern segment of the southern Lhasa

144 subterranean, the Yeba Formation volcano-sedimentary strata comprise a bimodal
145 volcanic suite with interbedded fine-grained sandstone, calcic slate, and limestone
146 (Wei et al., 2017; Zhu et al., 2008). Two samples were collected from the fine-grained
147 sandstones exposed ~30km north of the Sangri County (Fig. 1B). These samples are
148 quartzose sandstone and are composed of subangular monocrystalline quartz, lithic
149 fragments and argillaceous cement with average modal composition of
150 Q/F/L=88/2/10 (Table S1; Fig. 3), where Q, F and L refer to quartz, feldspar and
151 lithics, respectively.

152 **2.2.2 Chumulong Formation**

153 Five mudstone samples were collected from the Chumulong Formation north of
154 Shannan city (Fig. 1B). The Chumulong Formation is dominated by dark-grey
155 mudstone with subordinate siltstone and sandstone. The mudstone is interbedded with
156 very fine-grained bioturbated sandstone with oyster fragments and fossil wood debris
157 (Fig. 2). This lithofacies association is interpreted as being deposited in a lagoon
158 environment (Leier et al., 2007a).

159 **2.2.3 Shexing Formation**

160 Eight sandstone samples were collected from the Shexing Formation red beds
161 (Fig. 2) northwest of Lhasa city (Figs. 1B). The sandstone units sampled are part of
162 a >2km-thick, strongly folded fluvial clastic succession which is covered by the

163 undeformed Paleogene Linzizong Group volcanic succession (LVS; Mo et al., 2008).
164 These sandstones are feldspathic arenite and show large modal composition variations
165 with average Q/F/L=35/27/38 (Table S1; Fig. 3).

166 **2.2.4 Ngamring Formation**

167 The flysch sequence of Ngamring Formation consists of alternating beds of
168 sandstone and mudstone (Fig. 2) and is characterized by a series of large channelized
169 conglomerates in the lower portion (Wang et al., 2012). Based on stratigraphy,
170 sandstone petrography and detrital zircon age population, the Ngamring Formation
171 can be further divided into three subsequences, i.e., the Lower, Middle and Upper
172 Ngamring Formations (An et al., 2014; Wu et al., 2010). Eight samples were collected
173 from the sandstone beds, among which RK1601, RK1602, RK1603 and RK1605 are
174 from the Lower Ngamring Formation, RK1612 and RK1613 are from the Middle
175 Ngamring Formation, and RK1614 and RK1615 are from the Upper Ngamring
176 Formation. The samples are litharenite to feldspathic arenite and contain a large
177 number of volcanic fragments (Table S1; Fig. 3) with average modal composition of
178 Q/F/L=12/23/65.

179 **3 Methods**

180 Modal composition analysis was carried out on eighteen sandstone samples with
181 300 points counted per thin section using Gazzi-Dickinson method (Ingersoll et al.,

182 1984). The results are plotted in Fig. 3 and given in Table S1.

183 Detrital zircons were extracted from crushed samples using heavy liquid and
184 magnetic separation techniques. Individual grains were handpicked, mounted in epoxy
185 resins and then polished to expose the interiors. Zircon U-Pb ages were measured using
186 LA-ICPMS at State Key Laboratory of Geological Processes and Mineral Resources
187 (GPMR), China University of Geosciences, Wuhan, by following Liu et al. (2010a).
188 Cathodoluminescence (CL) images were not referenced and all analyzed grains were
189 selected randomly from all sizes and shapes during the analysis. The laser spot was 32
190 microns in diameter and always placed on the center of the zircon grain. Zircon
191 standard 91500 was analyzed as external standard to correct for Pb isotope
192 fractionation. Offline data calculations were processed using the program
193 ICPMSDataCal_Ver8.0 (Liu et al., 2010b). The ages presented in this study are
194 $^{206}\text{Pb}/^{238}\text{U}$ ages for zircons $< 1000\text{Ma}$ and $^{207}\text{Pb}/^{206}\text{Pb}$ ages for those $>1000\text{Ma}$. The
195 analyses with more than 20% discordance are omitted from further discussion. The
196 kernel density estimation (KDE) plots were constructed using the software
197 DensityPlotter (Vermeesch, 2012). Analyzed as an unknown, the zircon standard
198 Plesovice yielded a mean $^{206}\text{Pb}/^{238}\text{U}$ age of $338\pm 0.6\text{Ma}$ (2σ , $n=117$).

199 Maximum depositional age is determined using method of Dickinson and Gehrels
200 (2009), who suggest both YSG (youngest single grain age) and $\text{YC}1\sigma(2+)$ (weighted
201 mean age of youngest detrital zircon cluster with two or more grains overlapping in age
202 at 1σ) show similar compatibility with depositional age, but the former may be

203 suspicious due to inherent lack of reproducibility. The $YC2\sigma(3+)$ (weighted mean age
204 of youngest detrital zircon cluster with three or more grains overlapping in age at 2σ) is
205 the most conservative measurement and considerably older than depositional age.
206 Generally, $YC1\sigma(2+)$ is preferred as maximum depositional age. In this study, the YSG
207 is suggested for those whose $YC1\sigma(2+)$ are inconsistent with the depositional ages
208 determined via other samples/methods. Detrital zircon U-Pb data are summarized in
209 Table 1 and plotted in Fig. 4.

210 In-situ zircon Hf isotope analysis was conducted using LA-MC-ICPMS in the
211 Institute of Geology and Geophysics, Chinese Academy of Sciences (IGGCAS). Zircon
212 grains were ablated using a 193nm excimer ArF laser (GeoLas Plus) with a spot
213 diameter of 45-60 microns. Ablated material was carried by helium and introduced into
214 a Neptune MC-ICPMS. The analytical details were given by Wu et al. (2006). The
215 U-Pb dating and Hf isotope raw data are present in Tables S2 and S3.

216 Whole rock major and trace element analyses were carried out at GPMR, Wuhan.
217 Major element oxide measurement was done using a SHIMADZU sequential X-ray
218 fluorescence spectrometer (XRF-1800) following Ma et al. (2012). The analytical
219 uncertainties are better than 3%. Trace elements were determined using an Agilent
220 7500a ICP-MS by following Liu et al. (2008). The analytical results are presented in the
221 Table S4.

222 **4 Results**

223 **4.1 Detrital zircon geochronology and Hf isotope**

224 **4.1.1 Yeba Formation**

225 A total of 104 usable detrital zircon ages show a large variation from 179 ± 2 to
226 3520 ± 20 Ma (Figs. 4A, 4B). Pre-Mesozoic ages comprise the largest population (99 out
227 of 104 results), which form significant peaks centered at 556 and 1170Ma. The
228 depositional interval age has been yielded to Early-Middle Jurassic (~ 168 -192Ma) via
229 zircon geochronologic study on the volcanic sequences within the Yeba Formation
230 strata (Liu et al., 2018; Wei et al., 2017; Zhu et al., 2008). Therefore, although the
231 $YC1\sigma(2+)$ and $YC2\sigma(3+)$ of sample D54 was yielded to 563.5 ± 3.6 and 248.0 ± 3.5 Ma,
232 respectively, the maximum depositional age is supposed to be 179Ma using the
233 youngest single zircon grain age (YSG).

234 **4.1.2 Chumulong Formation**

235 The four Chumulong samples yield 327 usable ages (Figs. 4C, 4D). Sample D47A
236 yields 103 usable ages ranging from 117 ± 1 to 2595 ± 14 Ma with major peaks at 121 and
237 224Ma. Sample D47B yields 109 usable ages ranging from 105 ± 1 to 2732 ± 29 Ma,
238 which form four peaks at 123, 143, 166 and 226Ma. Only 47 usable ages are obtained
239 from sample D47E, among which the largest population peaks at 231Ma. Among the 68
240 available analyses for the sample D47C, zircons with Paleozoic ages are predominant

241 (63 out of 68 results) with significant age peaks at 404 and 454Ma. The maximum
242 depositional age for the Chumulong Formation is recommended to be 121Ma using the
243 $YC1\sigma(2+)$ of sample D47A.

244 In-situ Hf isotope analysis was performed on 208 zircon grains that had not been
245 exhausted after the U-Pb age analysis. Zircon grains with Mesozoic ages display a large
246 variation in $^{176}\text{Hf}/^{177}\text{Hf}$ ratios with $\epsilon\text{Hf}(t)$ ranging from -24.3 to +14.7, revealing the
247 source rock diversity (Fig. 5).

248 **4.1.3 Shexing Formation**

249 The four Shexing samples yield 377 usable ages (Figs. 4E, 4F). Sample MX1102
250 yields 113 usable ages with the youngest being 84 ± 2 Ma. This sample contains a large
251 population of pre-Mesozoic zircons peaking at 550, 700, 1450, 1750 and 2600Ma,
252 whereas Mesozoic ages are subordinate (28 out of 113 results) with peaks at 88 and
253 121Ma. Sample MX1104 yields 90 usable ages that exhibit a major peak at 90Ma and a
254 subordinate at 112Ma. Sample MX1106 yields 86 usable ages with the youngest being
255 82 ± 2 Ma. Mesozoic zircons are predominant (71 out of 86 spots) showing a major peak
256 at 88Ma and a subordinate at 201Ma. Sample MX1108 yields 88 usable ages, most of
257 which are pre-Mesozoic (82 out of 88 spots). Only four grains are identified with
258 Cretaceous ages of 91 ± 2 Ma, 92 ± 2 Ma, 105 ± 4 Ma and 121 ± 5 Ma. This sample yielded
259 numerous small clusters and scatters showing no significant peaks. The maximum
260 depositional age for the Shexing Formation is supposed to be 88Ma using the $YC1\sigma(2+)$

261 of sample MX1106.

262 Mesozoic zircons from these samples exhibit varying Hf isotope composition (Fig.
263 5). Zircons with ages <105Ma have high $^{176}\text{Hf}/^{177}\text{Hf}$ ratios with $\epsilon_{\text{Hf}}(t)$ ranging from -0.6
264 to +13.7, whereas those with ages between 109 and 238Ma show varying $^{176}\text{Hf}/^{177}\text{Hf}$
265 with $\epsilon_{\text{Hf}}(t)$ ranging from -16.1 to +5.4.

266 4.2 Bulk-rock geochemistry

267 4.2.1 Major elements

268 The Yeba and Chumulong samples as a whole display higher compositional
269 maturity than those of the Ngamring and Shexing Formations. In terms of major
270 oxides, the Yeba sandstones are potassic ($\text{K}_2\text{O}/\text{Na}_2\text{O}=5.64\text{-}7.04$) with higher SiO_2 ,
271 lower Al_2O_3 , and Na_2O (Figs. 6B, 6D and 6F). The Chumulong mudstones have
272 similar SiO_2 ($63.82\pm 5.90\text{wt.}\%$) but higher Al_2O_3 ($19.06\pm 2.26\text{wt.}\%$) relative to the
273 average composition of the upper continental crust ($\text{SiO}_2\sim 66.3\text{wt.}\%$, $\text{Al}_2\text{O}_3\sim 14.9\text{wt.}\%$;
274 Rudnick and Gao, 2003). Compared with those of the Yeba Formation, the Shexing
275 sandstones are typically sodic ($\text{K}_2\text{O}/\text{Na}_2\text{O}=0.16\text{-}0.57$, except for sample MX1103
276 ~ 1.14) and have a wider range of SiO_2 , Al_2O_3 and CaO abundances (Figs. 6B and 6E).
277 Similarly, the Ngamring samples display sodic characteristics ($\text{K}_2\text{O}/\text{Na}_2\text{O}=0.12\text{-}0.58$)
278 with relatively low SiO_2 ($55.9\pm 13.4\text{wt.}\%$). The high LOI values of the Ngamring
279 samples (4.37-10.29 wt.%) are attributed to the presence of detrital carbonate in terms
280 of petrographic observation and the positive CaO -LOI correlation ($r=0.97$). Generally,

281 in the sandstones, there are marked negative correlations of SiO_2 with TiO_2 , Al_2O_3 ,
282 $\text{MgO}+\text{Fe}_2\text{O}_3^{\text{T}}$ (where $\text{Fe}_2\text{O}_3^{\text{T}}$ represents total Fe as Fe_2O_3) and Na_2O (Figs. 6A, 6B,
283 6C, 6E and 6F), reflecting increasing compositional maturity towards high SiO_2 . It is
284 noted that Mg, Fe, Ti and Na largely reside in the volcanic lithic fragments, reflected
285 by the negative correlation of modal volcanic lithics proportion with these elements
286 (Figs. 6G, 6H and 6I).

287 4.2.2 Trace elements

288 All the samples have subparallel REE patterns (Fig. 7). The Yeba and Chumulong
289 samples show smoothly fractionated patterns with La/Yb_N of 7.23 – 15.2 (where
290 subscript N refers to chondrite-normalized values) and Eu/Eu^* of 0.55 – 0.72. The
291 former has lower ΣREE (refers to total REE) abundances (99 ± 28 ppm) than the latter
292 (180 ± 30 ppm) due to quartz dilution effect. The Shexing samples have similar REE
293 distributions ($\text{La}/\text{Yb}_N=8.09-10.2$) but weak or absent Eu anomalies
294 ($\text{Eu}/\text{Eu}^*=0.63-1.00$) with lower ΣREE abundances (125 ± 44 ppm). The Ngamring
295 samples are characterized by relatively flat patterns with lowest La/Yb_N ratios
296 (4.10-8.39), ΣREE abundances (74 ± 21 ppm) and Eu/Eu^* ranging from 0.77 to 1.05.
297 In the sandstone samples, Eu/Eu^* is most likely controlled by the enrichment of
298 plagioclase-rich volcanic lithic fragments (Fig. 6L). This suggests that these samples
299 were deposited in a volcanically active region with short transport distance of the
300 clastics.

301 In the upper continental crust normalized multielement diagram (Fig. 7E),
302 patterns of the Shexing and Ngamring samples are subparallel to the unweathered
303 Yeba volcanic rocks (except for individual element), which are concordant with
304 predominant magmatic provenances. The Yeba and Chumulong samples show
305 gradually reduced depletion in the order of Na, Sr, Ba and K. Rb is enriched in the
306 Chumulong mudstones probably due to the adsorption by clays. The transition metals
307 (Co, Ni, Cr, and V) are largely inherited from the volcanic lithic fragments (Fig. 6J) in
308 the sandstone samples. Th and U are generally coherent during most magmatic
309 processes; however, they may be fractionated during weathering and sedimentary
310 recycling processes. The Ngamring, Shexing, Yeba and Chumulong samples have
311 gradually increasing Th/U ratios of 3.14 ± 1.47 , 4.66 ± 1.09 , 4.91 ± 0.31 and 6.04 ± 0.76 ,
312 respectively. See below for detailed discussion.

313 **5 Influence of sedimentary processes on elemental variations**

314 Chemical composition of terrigenous sedimentary rocks is the net result of
315 various factors, which includes provenance, weathering, sorting, diagenesis and
316 post-depositional metamorphism. Each of these processes should be taken into
317 account when speculating tectonic implications using geochemical data. It is
318 suggested that the Yeba Formation has undergone up to greenschist-facies
319 metamorphism (Wei et al., 2017; Zhu et al., 2008). In this case, the unweathered Yeba
320 Formation volcanic rocks with greenschist-facies metamorphism are introduced into

321 the next discussion for estimating the influence of metamorphism on the
322 compositional variation of the clastic rock samples.

323 **5.1 Weathering and diagenesis**

324 Chemical weathering modifies the composition of rocks via water-rock
325 interaction. With increasing intensity of chemical weathering, there is typically an
326 increase in clays at the expense of unstable components such as volcanic lithic
327 fragments, ferromagnesian minerals and feldspars. Meanwhile, the soluble alkali or
328 alkaline-earth metals (AAEM) with smaller ionic radius tends to be preferentially
329 leached from the soils than the larger one that is more readily retained on exchange
330 sites of clay minerals (McLennan et al., 1993). The Yeba and Chumulong clastic
331 samples show an increasing depletion tendency towards the smaller AAEM cations
332 (Fig. 7E), indicating that their precursors were subjected to significant chemical
333 weathering. Compared with the clastic rock samples, the Yeba volcanic rocks show a
334 distinct AAEM pattern with high Na and Sr abundances, suggesting the regional
335 metamorphism has played no dominant role in modifying the AAEM composition of
336 the Yeba Formation. In contrast, the AAEM patterns of the Shexing and Ngamring
337 clastic samples are similar to that of the Yeba Formation volcanic rocks (Fig. 7E),
338 revealing that the source rock disaggregation was primarily controlled by physical
339 weathering with restricted chemical modification.

340 To better quantify the degree of chemical weathering, Chemical Index of

341 Alteration (CIA) is used here (Nesbitt and Young, 1982): $CIA = \frac{Al_2O_3}{[Al_2O_3 + K_2O +$
342 $Na_2O + CaO^*]} \times 100$, where CaO^* refers to that residing in silicate minerals only. In
343 this case, a correction should be made through subtracting the CaO from carbonate
344 and apatite. In this study, the CaO is preferentially corrected for apatite using
345 bulk-rock P_2O_5 abundance (mole $CaO_{corr} = \text{mole } CaO - \text{mole } P_2O_5 \times 10/3$). If the
346 mole CaO_{corr} is less than Na_2O , its value is adopted as the CaO^* ; otherwise the CaO^*
347 value is assumed to be equivalent to Na_2O (McLennan et al., 1993; Yan et al., 2010).
348 The CIA value is directly related to chemical weathering intensity, from 50 in
349 unweathered igneous rocks to 100 in residual clays. According to the existing data
350 (Wei et al., 2017), the Yeba volcanic rocks with greenschist-facies metamorphism
351 have a mean CIA value of ~50, confirming that the post-depositional metamorphism
352 had not significantly increased the CIA values of the Yeba Formation rocks. For better
353 visualizing the significance of CIA values, the samples are plotted on the A-CN-K
354 ternary diagram (Fig. 8A). The Yeba and Chumulong samples show moderate to high
355 degree of chemical weathering with CIA values ranging from 71 to 81, which are
356 significantly higher than the Yeba volcanic rocks but similar to that of the typical
357 shale (~70-75; Taylor and McLennan, 1985). The Shexing and Ngamring samples
358 have lower CIA values of 49 to 59, revealing limited chemical modification and short
359 distance transportation of the clastics. All the samples fall on a trend deviating from
360 that of diagenetic K-metasomatism (smectite-illite transformation; Fedo et al., 1995),
361 but consistent with weathering being the sole control (McLennan et al., 1993). When

362 plotted in A-CNK-FM ternary diagram (Fig. 8B), the samples show trends that are
363 best understood as mixing sources. These results further indicate that the CIA values
364 of the clastic samples were decoupled from the compositional variation of their
365 precursors.

366 Another geochemical index, Th/U, is commonly used to estimate the impact of
367 chemical weathering (McLennan et al., 1993; Taylor and McLennan, 1985). In most
368 cases, chemical weathering under oxidizing environment can transform U^{4+} to more
369 soluble U^{6+} . The subsequent dissolution and loss of U^{6+} results in elevation of Th/U in
370 clastic rocks, especially for mudstones and shales, where heavy minerals are less
371 likely to be an interfering factor (McLennan et al., 1993). It appears that the data
372 follow the trend consistent with weathering being the primary control (Fig. 9);
373 however, the Yeba samples show indistinguishable Th/U ratios and Th abundances
374 from the Shexing counterparts, which contradict their distinct CIA values. It is also
375 noted that the Th/U ratios in the sandstone samples overlap with those of the Yeba
376 volcanic rocks (Fig. 5C) and are proportional to the content of volcanic lithics (Fig.
377 3K). Therefore, we suggest that Th/U ratios of the sandstones largely reflect the
378 nature of the provenance rocks rather than the extent of chemical weathering.

379 **5.2 Hydraulic sorting**

380 The most commonly used approach to examine the influence of sorting on
381 sedimentary rocks is to evaluate the textural maturity using characteristic grain sizes

382 and shapes (McLennan et al., 1993). Sorting processes are usually accompanied by
383 fractionation or enrichment of heavy minerals (notably zircon), which can
384 significantly modify abundances of the elements that are at trace levels in most
385 sedimentary rocks (e.g., Zr and Hf in zircon). Therefore, geochemical composition of
386 clastic rocks is also useful in evaluating the impact of sorting. Zr/Sc ratio is a
387 promising tracer for zircon accumulation, since Zr is mostly concentrated in zircon
388 whereas Sc is not enriched but generally inherited from the precursors. Th/Sc ratio is
389 suggested as a potential indicator of magmatic differentiation, because Th behaves
390 conservative during sedimentary processes (McLennan et al., 1993). In most of the
391 samples, Zr/Sc covaries with Th/Sc, which can be attributed to compositional
392 variation of the precursors. Note that the Chumulong samples show some variation in
393 Zr/Sc with unvarying Th/Sc (Fig. 10A). Generally, fine-grained clastic rocks such as
394 shales and mudstones are deposited in low-energy environment so that they are less
395 prone to accumulating zircon. In this case, the Zr/Sc variations in the Chumulong
396 samples are best understood as a consequence of hydraulic sorting. Considering that
397 zircon is a weathering-resistant mineral with high density, its fractionation during
398 sedimentary processes reveals a long-distance transportation of the clastic materials
399 before deposition. The other sandstone samples lie on the trend that is consistent with
400 compositional variations of the source rocks, indicating insignificant zircon
401 fractionation. In some sediments of mineralogical immaturity, sorting can result in
402 accumulation of plagioclase and volcanic fragments (McLennan et al., 1993). In the

403 Ngamring and Shexing sandstones, the Eu/Eu^* is most likely controlled by the
404 enrichment of plagioclase-rich volcanic lithic fragments (Fig. 3L), suggesting that the
405 samples were deposited in a volcanically active region with short distance
406 transportation of the clastic materials.

407 **5.3 Two-component mixing model**

408 Elements having conservative behavior in sedimentary processes and low
409 residence time in seawater, such as Th, Nb, Zr, Co, Sc and LREEs, are promising
410 indicators for the source rock signature (Bhatia and Crook, 1986). In the Th-Sc-Zr/10
411 ternary diagram (Fig. 10A), most of the samples show compositional similarity to the
412 clastic rocks from oceanic or continental arcs. The Chumulong samples show a linear
413 trend away from the Zr/10 apex, consistent with the fact that mudstones are depleted
414 in zircon due to sorting. In the Fig. 10B, the samples plotted in the array of Gangdese
415 magmatic arc, likely signifying mixing of two endmembers (mafic and silicic source
416 rocks). A diagram of La/Sc vs. Co/Th (Fig. 11) is constructed to further test the
417 two-component mixing model. All the data points lie on the mixing curve and show
418 good agreement with the bimodal mixing model. The Ngamring samples display
419 largest compositional variations, among which RK1605 with lowest SiO_2 abundance
420 (46.7 wt.%) and highest Co/Th ratio (21.2) requires >90% mafic component
421 contribution. This result is concordant with the petrographic observation showing a
422 large proportion of basaltic lithic fragments in the Ngamring samples, and reveals that

423 the low SiO₂ abundances of the Ngamring samples are not attributed to the presence
424 of carbonate characterized by low Co/Th ratio. The Shexing samples have overall
425 intermediate to silicic provenance with >50% silicic component contribution. The
426 Yeba and Chumulong sediments have most acidic provenance with >80% silicic
427 component.

428 **6 Sedimentary provenances and tectonic implication**

429 **6.1 Yeba Formation (~192-168Ma)**

430 The Yeba sandstones are characterized by high CIA values and significant
431 negative Eu/Eu* anomalies (Fig. 7) with strong depletion in alkali and alkaline earth
432 metals (Fig. 7E), indicating a low-relief provenance with tropical climate. According
433 to the mixing model (Fig. 11), the Yeba sandstones are best interpreted as being
434 sourced from silicic provenance. Petrographic observation shows that the modal
435 compositions of the Yeba samples fall into the recycled orogen region in the Q-F-L
436 plot (Fig. 3). Detrital zircon data reveal that the Yeba Formation sediments were
437 recycled from the pre-Jurassic strata in the Lhasa terrane without exotic clastic
438 addition, because: (1) the Mesozoic ages are relatively rare (~5.7%, 6 out of 104 results)
439 in the sample D54, suggesting a limited supply of juvenile materials; and (2) the age
440 spectrum is subparallel to those of the Paleozoic and Triassic metasedimentary rocks
441 (notable age peak of ~1170Ma; Figs. 13B, 13C, 13D) in the Lhasa terrane but distinct
442 from those of the western Qiangtang clastic rocks (characterized by significant peak

443 of ~950Ma; Fig. 13G). These results suggest that the Lhasa terrane was an isolated
444 geological block drifting in the Tethyan ocean and had not collided with the
445 Qiangtang terrane during the Early Jurassic.

446 Previous research has suggested that subduction zones were developed on both
447 northern and southern sides of the Lhasa terrane (Zhu et al., 2013; 2016). Substantial
448 Triassic-Jurassic subduction-related volcanism (237-168Ma) occurred in the southern
449 Lhasa subterrane (e.g., Kang et al., 2014; Liu et al., 2018; Tafti et al., 2014; Wang et
450 al., 2016; Wei et al., 2017) indicates that the northward subduction of the
451 Neo-Tethyan oceanic lithosphere beneath the Lhasa terrane should initiate prior to the
452 Middle Triassic (Wang et al., 2016). An alternative view presumed that the Early
453 Mesozoic magmatism was induced by southward subduction and rollback of the
454 Bangong Tethyan oceanic lithosphere (Zhu et al., 2013). It is noted that the
455 Triassic-Jurassic subduction-related volcanism exposed in the area ~250-300km south
456 of the Bangong Suture without considering ~60% crustal shortening occurring during
457 the Late Jurassic – Cretaceous (Murphy et al., 1997). However, the mean distance
458 from arc volcanoes to trench in the modern subduction zones is 166 ± 60 km (Stern,
459 2002). In this case, it is more reasonable that the volcanisms in southern Lhasa terrane
460 were associated with northward subduction of the Neo-Tethyan oceanic lithosphere.

461 In the southern Lhasa terrane, the subduction-related Xiongcu porphyry Cu
462 deposit with ore-bearing country rocks of the Early-Middle Jurassic Xiongcu
463 Formation volcano-sedimentary sequence was developed to the west of the Yeba

464 Formation (Lang et al., 2014, 2018; Tafti et al., 2009; 2014; Tang et al., 2015). Sillitoe
465 (1998) favored the compressional regime for the formation of subduction-related
466 porphyry Cu deposits in terms of the statistic study on global Cu deposits; however,
467 no Cu deposits have been found in the Yeba Formation, which was previously
468 considered to be formed in continental arc setting (Zhu et al., 2008). The Xiongkun
469 sandstones are classified as lithic arenite and have modal composition of
470 Q/F/L=21:11:68 (Fig. 3) with positive detrital zircon Hf isotopic fingerprints (+10.5
471 to +16.2) (Lang et al., 2018). These results indicate that the Xiongkun and Yeba
472 sandstones were deposited in different tectonic settings. The high proportion of
473 volcanic lithic fragments reveals that the Xiongkun sandstones were sourced from
474 uplifting volcanic arcs, while the high degree of chemical weathering (CIA =77-85)
475 suggests a tropical climate (Lang et al., 2018). The Yeba sandstones, however, are
476 predominated by recycled quartz and underwent high chemical weathering, indicating
477 that they were gradually deposited in the basin with relatively subdued uplift and low
478 elevations (Fig. 14A). A reasonable explanation is that the Yeba Formation was
479 deposited in the back-arc basin close to the central Lhasa terrane, whereas the
480 Xiongkun Formation represents the Gangdese volcanic arc front. The southern margin
481 of the Lhasa terrane most likely resembles the present-day Ryukyu-Okinawa arc-basin
482 system in the Early-Middle Jurassic. This proposal is reinforced by the study on the
483 volcanic rocks suggesting the Yeba Formation were formed in extensional setting (Liu
484 et al., 2018; Wei et al., 2017).

485 6.2 Chumulong Formation (~121-105Ma)

486 In this study we calculate a maximum depositional age of 121Ma for the
487 Chumulong Formation, which is ~22Myrs younger than reported in Leier et al.
488 (2007c). The Chumulong samples have similar geochemical characteristics to the
489 Yeba Formation counterparts (i.e., high CIA values, low Na₂O/K₂O, strong depletion
490 in Na⁺ and Sr²⁺ and significant negative Eu anomalies; Figs. 7E and 12), revealing a
491 high degree of chemical modification during weathering and clastic transportation
492 processes. Taking into account that the Chumulong Formation is dominated by
493 mudstones and subordinate fine-grained sandstones accompanied with fossil wood
494 debris, we suggest that the climate and relief were not markedly changed from the
495 Jurassic and the southern Lhasa terrane maintained at low elevations (Fig. 13C).

496 Note that detrital zircon data indicate that source regions of the Early Cretaceous
497 sediments were inconsistent with the pre-Cretaceous samples. Firstly, detrital zircon
498 age peak of ~950Ma appears in the Early Cretaceous samples (Fig. 12E). Secondly,
499 the Early Cretaceous samples show insignificant age population around ~1170Ma,
500 which differs from those of the pre-Cretaceous samples. These results strongly imply
501 a Middle-Late Jurassic tectonic event that could result in the change of source region
502 of the sediments in the Lhasa terrane. One of the most significant tectonic events for
503 the Lhasa terrane prior to the India-Asia collision is its collision with the Qiangtang
504 terrane, which was speculated to initiate as early as the Middle Jurassic (Lai et al.,
505 2019; Li et al., 2019; Sun et al., 2019) and completed during the Late Jurassic to Early

506 Cretaceous (Zhu et al., 2016). The discrepancies of detrital zircon age spectra between
507 the pre-Cretaceous and Cretaceous samples are best interpreted as resulting from the
508 Lhasa-Qiangtang collision. As a consequence, a foreland basin was probably formed
509 in the Lhasa terrane (Figs. 13B) and clasts from Qiangtang were transported to the
510 Lhasa terrane by south-directed rivers. This proposal is supported by the appearance
511 of the Berriasian-Valanginian (~145-134Ma) foreland molasse association in the
512 central Lhasa terrane with paleocurrent directions mainly toward the south (Zhang et
513 al., 2012).

514 However, a simple foreland basin model is probably insufficient to explain the
515 sedimentary records in the northern Lhasa terrane. During the Early Cretaceous,
516 extensive volcanism (i.e., Zenong Group; Zhu et al., 2011a) occurred in the northern
517 Lhasa terrane and overprinted the foreland basin in some localities. Subordinate
518 basins (e.g., Coqen and Selin Co basins; Sun et al., 2017; Zhang et al., 2011) were
519 consequently formed with deposition of the Duoni Formation. Sun et al. (2017)
520 suggested that the Duoni Formation was mainly sourced from the Zenong volcanic
521 rocks and basement rocks from the southern portion of the northern Lhasa subterrane.
522 It is also noted that the detrital zircons from the Duoni clastic rocks exhibit significant
523 age peaks of 950 and 1170Ma (Leier et al., 2007c; Zhang et al., 2011), similar to those
524 of the Early Cretaceous samples in the southern Lhasa terrane (Fig. 12E). Furthermore,
525 the detrital zircons are characterized by negative $\epsilon_{\text{Hf}}(t)$ (Fig. 5), implying no sediment
526 supply from the Gangdese magmatic arc to the south. Paleocurrents measured from

527 Duba section of the Duoni Formation and Linzhou section of the Chumulong
528 Formation are overall south-directed, although few of them indicate north-directed
529 flows (Leier et al., 2007a). Considering all the geological evidences, we suggest that
530 clastic contribution from the Qiangtang terrane cannot be precluded in the Early
531 Cretaceous sedimentary basins of the northern Lhasa terrane, and the Lhasa terrane
532 was still a south-dipping foreland basin as a whole. This model is consistent with the
533 study of Wang et al., (2017b) on Damxung conglomerates in the central Lhasa terrane,
534 who suggested the initial topographic growth took place in the northern part of the
535 Lhasa terrane by the early Albian time. A composite foreland basin model (Fig. 14C)
536 is suitable, where multiple subordinate sedimentary basins were developed with
537 clastic materials coming from both the Qiangtang terrane and the interiors of the
538 Lhasa terrane.

539 **6.3 Ngamring Formation (~104-83Ma)**

540 As the first and main turbiditic fill of the Xigaze forearc basin (An et al., 2014;
541 Wang et al., 2012), the Ngamring Formation is in conformable contact with
542 underlying deep-water sediments of the Chongdui Formation (Wang et al., 2017a).
543 The change of lithofacies association from deep-water sediments to turbidites indicate
544 a late Early Cretaceous tectonic event occurred along the southern margin of the
545 Lhasa terrane. Overall, the Ngamring sandstones are characterized by low CIA values,
546 high $\text{Na}_2\text{O}/\text{K}_2\text{O}$ and weak to absence of Eu anomalies, displaying high compositional

547 and textural immaturity (Fig. 12). The Lower Ngamring Formation is supposed to
548 have a maximum depositional age of 104Ma (An et al., 2014). The Lower Ngamring
549 samples are characterized by low SiO₂ and high Na₂O/K₂O, from which detrital
550 zircons are predominately of Cretaceous age with positive εHf(t) values (An et al.,
551 2014; Wu et al., 2010). According to the two-component mixing model (Fig. 11),
552 significant contribution of mafic component (40-92%) is required for the Ngamring
553 sandstones. These results reveal that the Gangdese magmatic arc was in a period of
554 strong volcanic activities, consistent with the petrographic observation showing
555 abundant volcanic lithic fragments in the Ngamring samples. Therefore, we advocate
556 that the Gangdese magmatic arc was quickly uplifting above sea level (Fig. 14D) and
557 changing the shelf and submarine canyon morphology since the late Early Cretaceous.
558 Leier et al. (2007b) drew a similar conclusion via addressing the sandstone
559 provenance of the age-equivalent Takena Formation in the north of the Gangdese
560 magmatic arc. Samples of the Middle Ngamring Formation (~99-88Ma; An et al.,
561 2014) have higher SiO₂ and lower Na₂O/K₂O than the Lower Ngamring counterparts
562 indicating an additional supply of dissected magmatic arc materials. This inference
563 can be verified by the appearance of older detrital zircons peaking at ~157Ma with
564 positive εHf(t) values in the Middle Ngamring sandstones (An et al., 2014; Wu et al.,
565 2010). This means that by this time the south-flowing rivers had penetrated the
566 Gangdese magmatic arc. Samples of the Upper Ngamring Formation (~88-84Ma; An
567 et al., 2014; Wu et al., 2010) are the most acidic with lowest Na₂O/K₂O, showing

568 diversity of the source rocks. Abundant pre-Cretaceous detrital zircons with large
569 variation of $\epsilon_{\text{Hf}}(t)$ values in the Upper Ngamring sandstones suggest the sediments be
570 transported from the northern portion of the Lhasa terrane or even from the Qiangtang
571 terrane. The expansion of river catchments was most likely to be the result of regional
572 uplift of the northern Lhasa and Qiangtang terranes during the Late Cretaceous.
573 Above all, the Ngamring Formation turbidites record the denudation of the Gangdese
574 magmatic arc, which reflects uplifting history of the southern margin of the Lhasa
575 terrane.

576 **6.4 Shexing Formation (~87-72Ma)**

577 It is suggested that deposition of the Shexing Formation likely initiated by ~87Ma
578 constrained by detrital zircon geochronology in this study, and ended by ~72Ma
579 yielded by the volcanic rocks interbedded in the uppermost Shexing sequence (Sun et
580 al., 2012). Characterized by low CIA, $\text{K}_2\text{O}/\text{Na}_2\text{O}$, weak to absence of Eu anomalies
581 and large proportion of lithic grains, the Shexing sandstone samples illustrate a
582 tectonically active source region that was rapidly uplifting with surface rocks
583 disintegrated by physical weathering. Consider that the Lhasa terrane located at low
584 latitudes (~15°N) during the Late Cretaceous, a high altitude (cold climate) is required
585 to keep the chemical weathering intensity of the Shexing sandstones to a low level. A
586 counter example is the Xiongkun lithic arenite with high chemical weathering
587 intensity, which indicates the Lhasa terrane was at low elevation during the Jurassic. A

588 possible mechanism for the Late Cretaceous uplift of the Gangdese magmatic arc is
589 the Neo-Tethyan mid-ocean ridge subduction (Zhang et al., 2010). The positive $\epsilon_{\text{Hf}}(t)$
590 values of young detrital zircons ($<105\text{Ma}$) indicate that the Gangdese magmatic arc
591 serves as a main provenance. This inference is further supported by the paleocurrents
592 recording locally northward-flowing rivers during the Late Cretaceous (Leier et al.,
593 2007b). Considering that there are also abundant Mesozoic detrital zircons with
594 $\epsilon_{\text{Hf}}(t) < 0$ (Fig. 5), more sources in addition to the Gangdese magmatic arc are required
595 for the Shexing sandstones. Detrital zircon age spectrum of the Late Cretaceous
596 samples (Fig. 13F) shows more evident peaks of $\sim 800\text{Ma}$ and $\sim 950\text{Ma}$ than the Early
597 Cretaceous samples, revealing an increasing sediment supply from the Qiangtang
598 terrane during the Late Cretaceous.

599 These results reconcile that the Lhasa and Qiangtang terranes were uplifted
600 simultaneously during the Late Cretaceous (Fig. 14E). At the end of the Cretaceous,
601 the crust of the Lhasa terrane was likely thickened to approximately twice the normal
602 thickness prior to the India-Asia collision (Kapp et al., 2005, 2007; Murphy et al.,
603 1997; Zhu et al., 2017).

604 **7 Summary**

605 (1) Twenty-Three Jurassic-Cretaceous clastic rock samples from the southern
606 Lhasa terrane were analyzed for petrology and major and trace elements composition
607 with the aim of illustrating the possible tectonic evolution of the Lhasa terrane.

608 Overall, the samples from the Yeba and Chumulong Formations show higher
609 compositional maturity than those of the Ngamring and Shexing Formations. All the
610 samples display smooth REE patterns with LREE enrichment and varying Eu
611 anomalies.

612 (2) Sediments from the Jurassic-Early Cretaceous sequences (i.e., Yeba and
613 Chumulong Formations) show high textural and compositional maturity and
614 experienced moderate to high degree of chemical weathering, whereas those from the
615 Late Cretaceous sequences (i.e., Ngamring and Shexing Formations) are characterized
616 by low textural and compositional maturity and less affected by chemical weathering.

617 (3) Maximum depositional ages of the strata in the southern Lhasa terrane are
618 estimated to be 179Ma for the Yeba Formation, 121Ma for the Chumulong Formation
619 and 87Ma for the Shexing Formation. In-situ Hf isotope data show either positive or
620 negative $\epsilon\text{Hf}(t)$ for the detrital zircons with Mesozoic ages, revealing a joint
621 contribution of juvenile (from the Gangdese magmatic arc) and recycled (from the
622 Qiangtang terrane and the interiors of the Lhasa terrane) components to the
623 Cretaceous sediments in the southern Lhasa terrane.

624 (4) During the Early-Middle Jurassic (~192-168Ma), arc-basin system was
625 developed in the southern Lhasa terrane. The Middle Jurassic-Early Cretaceous
626 Lhasa-Qiangtang collision has resulted in the formation of a composite foreland basin
627 with southward-flowing rivers carrying clastic materials from the uplifted northern
628 Lhasa and/or Qiangtang terranes.

629 (5) From the late Early Cretaceous to Late Cretaceous (~104-72Ma), the
630 Gangdese magmatic arc was uplifted rapidly above the sea level, forming turbidites
631 (Ngamring Formation) in the Xigaze forearc basin and fluvial red beds (Shexing
632 Formation) on the retro-arc side. At the end of the Late Cretaceous, the entire Lhasa
633 terrane was likely to have been uplifted to high elevations forming an Andean-type
634 margin in the south before the India-Asia collision.

635 **Acknowledgements**

636 This study was financially supported by grants from the National Key R & D
637 Project of China (2016YFC0600304), the Natural Science Foundation of China
638 (41806080, 41602040), Shandong Provincial Key Laboratory of Depositional
639 Mineralization & Sedimentary Mineral (DMSM2018059), the Fundamental Research
640 Funds for the Central Universities (2652018122) and 111 project (B18048, B07011).
641 We are grateful for careful reviews by two anonymous reviewers, which greatly
642 helped us improve the paper. Editor M. Santosh was thanked for editorial handling.

643 **References**

- 644 An, W., Hu, X., Garzanti, E., Boudagher-Fadel, M.K., Wang, J., Sun, G., 2014. Xigaze
645 forearc basin revisited (South Tibet): Provenance changes and origin of the Xigaze
646 Ophiolite. *Geological Society of America Bulletin* 126, 1595-1613.
- 647 Bhatia, M.R., Crook, K.A.W., 1986. Trace element characteristics of graywackes and

- 648 tectonic setting discrimination of sedimentary basins. *Contribution to Mineralogy*
649 *and Petrology* 92, 181-193.
- 650 Cai, F., Ding, L., Laskowski, A.K., Kapp, P., Wang, H., Xu, Q., Zhang, L., 2016. Late
651 Triassic paleogeographic reconstruction along the Neo-Tethyan Ocean margins,
652 southern Tibet. *Earth and Planetary Science Letters* 435, 105-114.
- 653 Chung, S.-L., Lo, C.-H., Lee, T.-Y., Zhang, Y., Xie, Y., Li, X., Wang, K.-L., Wang, P.-L.,
654 1998. Diachronous uplift of the Tibetan plateau starting 40 Myr ago. *Nature* 394,
655 769.
- 656 Cohen, K.M., Finney, S.C., Gibbard, P.L., Fan, J.-X., 2013. The ICS International
657 Chronostratigraphic Chart. *Episodes* 36, 199-204.
- 658 Dickinson, W.R., 1985. Interpreting Provenance Relations from Detrital Modes of
659 Sandstones, in: Zuffa, G.G. (Ed.), *Provenance of Arenites*. Springer Netherlands,
660 Dordrecht, pp. 333-361.
- 661 Dickinson, W.R., Gehrels, G.E., 2009. Use of U-Pb ages of detrital zircons to infer
662 maximum depositional ages of strata: A test against a Colorado Plateau Mesozoic
663 database. *Earth and Planetary Science Letters* 288, 115-125.
- 664 Fedo, C.M., Wayne Nesbitt, H., Young, G.M., 1995. Unraveling the effects of
665 potassium metasomatism in sedimentary rocks and paleosols, with implications
666 for paleoweathering conditions and provenance. *Geology* 23, 921-924.
- 667 Fedo, C.M., Young, G.M., Nesbitt, H.W., 1997. Paleoclimatic control on the
668 composition of the Paleoproterozoic Serpent Formation, Huronian Supergroup,

- 669 Canada: a greenhouse to icehouse transition. *Precambrian Research* 86, 201-223.
- 670 Harrison, T.M., Copeland, P., Kidd, W.S.F., Yin, A., 1992. Raising Tibet. *Science* 255,
671 1663-1670.
- 672 Hou, Z., Duan, L., Lu, Y., Zheng, Y., Zhu, D., Yang, Z., Yang, Z., Wang, B., Pei, Y.,
673 Zhao, Z., 2015. Lithospheric Architecture of the Lhasa Terrane and Its Control on
674 Ore Deposits in the Himalayan-Tibetan Orogen. *Economic Geology* 110,
675 1541-1575.
- 676 Hu, X., Garzanti, E., Wang, J., Huang, W., An, W., Webb, A., 2016. The timing of
677 India-Asia collision onset – Facts, theories, controversies. *Earth-Science Reviews*
678 160, 264-299.
- 679 Ingersoll, R.V., Bullard, T.F., Ford, R.L., Grimm, J.P., Pickle, J.D., Sares, S.W., 1984.
680 The effect of grain size on detrital modes: a test of the Gazzi-Dickinson
681 point-counting method. *Journal of Sedimentary Research* 54, 103-116.
- 682 Kang, Z., Xu, J., Wilde, S.A., Feng, Z., Chen, J., Wang, B., Fu, W., Pan, H., 2014.
683 Geochronology and Geochemistry of the Sangri Group Volcanic Rocks, Southern
684 Lhasa Terrane: Implications for the Early Subduction History of the Neo-Tethys
685 and Gangdese Magmatic Arc. *Lithos* 200, 157-168.
- 686 Kapp, P., DeCelles, P.G., Gehrels, G.E., Heizler, M., Ding, L., 2007. Geological records
687 of the Lhasa-Qiangtang and Indo-Asian collisions in the Nima area of central
688 Tibet. *Geological Society of America Bulletin* 119, 917-933.
- 689 Kapp, P., Yin, A., Harrison, T.M., Ding, L., 2005. Cretaceous-Tertiary shortening, basin

- 690 development, and volcanism in central Tibet. *Geological Society of America*
691 *Bulletin* 117, 865-878.
- 692 Lai, W., Hu, X., Garzanti, E., Xu, Y., Ma, A., Li, W., 2019. Early Cretaceous
693 sedimentary evolution of the northern Lhasa terrane and the timing of initial
694 Lhasa-Qiangtang collision. *Gondwana Research* 73, 136-152.
- 695 Lang, X., Liu, D., Deng, Y., Tang, J., Wang, X., Yang, Z., Cui, Z., Feng, Y., Yin, Q., Xie,
696 F., Huang, Y., Zhang, J., 2018. Detrital zircon geochronology and geochemistry of
697 Jurassic sandstones in the Xiongcu district, southern Lhasa subterrane, Tibet,
698 China: implications for provenance and tectonic setting. *Geological Magazine* 156,
699 683-701.
- 700 Lang, X., Tang, J., Li, Z., Huang, Y., Ding, F., Yang, H., Xie, F., Zhang, L., Wang, Q.,
701 Zhou, Y., 2014. U–Pb and Re–Os geochronological evidence for the Jurassic
702 porphyry metallogenic event of the Xiongcu district in the Gangdese porphyry
703 copper belt, southern Tibet, PRC. *Journal of Asian Earth Sciences* 79, 608-622.
- 704 Leier, A.L., Decelles, P.G., Kapp, P., Gehrels, G.E., 2007a. Lower Cretaceous Strata in
705 the Lhasa Terrane, Tibet, with Implications for Understanding the Early Tectonic
706 History of the Tibetan Plateau. *Journal of Sedimentary Research* 77, 809-825.
- 707 Leier, A.L., Decelles, P.G., Kapp, P., Lin, D., 2007b. The Takena Formation of the
708 Lhasa terrane, southern Tibet: The record of a Late Cretaceous retroarc foreland
709 basin. *Geological Society of America Bulletin* 119, 31-48.
- 710 Leier, A.L., Paul, K., Gehrels, G.E., Decelles, P.G., 2007c. Detrital zircon

- 711 geochronology of Carboniferous–Cretaceous strata in the Lhasa terrane, Southern
712 Tibet. *Basin Research* 19, 361-378.
- 713 Li, S., Guilmette, C., Yin, C., Ding, L., Zhang, J., Wang, H., Baral, U., 2019. Timing
714 and mechanism of Bangong-Nujiang ophiolite emplacement in the Gerze area of
715 central Tibet. *Gondwana Research* 71, 179-193.
- 716 Li, Z., Lippert, P., Ding, L., Song, P., Yue, Y., Van Hinsbergen, D., 2016. Paleomagnetic
717 constraints on the Mesozoic drift of the Lhasa terrane (Tibet) from Gondwana to
718 Eurasia. *Geology* 44, 737-740.
- 719 Liu, Y., Gao, S., Hu, Z., Gao, C., Zong, K., Wang, D., 2010a. Continental and oceanic
720 crust recycling-induced melt–peridotite interactions in the Trans-North China
721 Orogen: U–Pb dating, Hf isotopes and trace elements in zircons from mantle
722 xenoliths. *Journal of Petrology* 51, 537-571.
- 723 Liu, Y., Hu, Z., Zong, K., Gao, C., Gao, S., Xu, J., Chen, H., 2010b. Reappraisal
724 and refinement of zircon U-Pb isotope and trace element analyses by LA-ICP-MS.
725 *Science Bulletin* 55, 1535-1546.
- 726 Liu, Y., Zong, K., Kelemen, P.B., Gao, S., 2008. Geochemistry and magmatic history of
727 eclogites and ultramafic rocks from the Chinese continental scientific drill hole:
728 subduction and ultrahigh-pressure metamorphism of lower crustal cumulates.
729 *Chemical Geology* 247, 133-153.
- 730 Liu, Z.C., Ding, L., Zhang, L.Y., Wang, C., Qiu, Z.L., Wang, J.G., Shen, X.L., Deng,
731 X.Q., 2018. Sequence and petrogenesis of the Jurassic volcanic rocks (Yeba

- 732 Formation) in the Gangdese arc, southern Tibet: Implications for the Neo-Tethyan
733 subduction. *Lithos* 312-313, 72-88.
- 734 Ludwig, K.R., 2003. User's manual for Isoplot 3.00: a geochronological toolkit for
735 Microsoft Excel. Berkeley Geochronology Center Special Publication.
- 736 Ma, Q., Zheng, J., Griffin, W., Zhang, M., Tang, H., Su, Y., Ping, X., 2012. Triassic
737 "adakitic" rocks in an extensional setting (North China): Melts from the cratonic
738 lower crust. *Lithos* 149, 159-173.
- 739 McLennan, S.M., Hemming, S., Mcdaniel, D.K., Hanson, G.N., 1993. Geochemical
740 approaches to sedimentation, provenance, and tectonics. Special Paper of the
741 Geological Society of America 284, 21-40.
- 742 Mo, X., Niu, Y., Dong, G., Zhao, Z., Hou, Z., Zhou, S., Ke, S., 2008. Contribution of
743 syncollisional felsic magmatism to continental crust growth: a case study of the
744 Paleogene Linzizong volcanic succession in southern Tibet. *Chemical Geology*
745 250, 49-67.
- 746 Molnar, P., Boos, W.R., Battisti, D.S., 2010. Orographic controls on climate and
747 paleoclimate of Asia: thermal and mechanical roles for the Tibetan Plateau.
748 *Annual Review of Earth and Planetary Sciences* 38, 77-102.
- 749 Murphy, M., Yin, A., Harrison, T., Dürr, S., Chen, Z., Ryerson, F., Kidd, W., Wang, X.,
750 Zhou, X., 1997. Did the Indo-Asian collision alone create the Tibetan plateau?
751 *Geology* 25, 719-722.
- 752 Nesbitt, H.W., Young, G.M., 1982. Early proterozoic climates and plate motions

- 753 inferred from major element chemistry of lutites. *Nature* 299, 715-717.
- 754 Nesbitt, H.W., Young, G.M., 1996. Petrogenesis of sediments in the absence of
755 chemical weathering: effects of abrasion and sorting on bulk composition and
756 mineralogy. *Sedimentology* 43, 341-358.
- 757 Pullen, A., Kapp, P., Gehrels, G.E., DeCelles, P.G., Brown, E.H., Fabijanic, J.M., Ding,
758 L., 2008. Gangdese retroarc thrust belt and foreland basin deposits in the
759 Damxung area, southern Tibet. *J. Asian Earth Sci.* 33, 323-336.
- 760 Richter, F.M., Rowley, D.B., Depaolo, D.J., 1992. Sr isotope evolution of seawater: the
761 role of tectonics. *Earth and Planetary Science Letters* 109, 11-23.
- 762 Rudnick, R.L., Gao, S., 2003. Composition of the Continental Crust, in: Holland, H.D.,
763 Turekian, K.K. (Eds.), *Treatise Geochem.* Pergamon, Oxford, pp. 1-64.
- 764 Sillitoe, R., 1998. Major regional factors favouring large size, high hypogene grade,
765 elevated gold content and supergene oxidation and enrichment of porphyry copper
766 deposits. *Porphyry and hydrothermal copper and gold deposits: A global
767 perspective: Adelaide, Australian Mineral Foundation*, 21-34.
- 768 Stern, R.J., 2002. Subduction zones. *Reviews of geophysics* 40, 3-1-3-38.
- 769 Sun, G., Hu, X., Sinclair, H., 2017. Early Cretaceous palaeogeographic evolution of the
770 Coqen Basin in the Lhasa Terrane, southern Tibetan Plateau. *Palaeogeography,
771 Palaeoclimatology, Palaeoecology* 485, 101-118.
- 772 Sun, G., Hu, X., Xu, Y., BouDagher-Fadel, M.K., 2019. Discovery of Middle Jurassic
773 trench deposits in the Bangong-Nujiang suture zone: Implications for the timing of

- 774 Lhasa-Qiangtang initial collision. *Tectonophysics* 750, 344-358.
- 775 Sun, Z., Pei, J., Li, H., Xu, W., Jiang, W., Zhu, Z., Wang, X., Yang, Z., 2012.
- 776 Palaeomagnetism of late Cretaceous sediments from southern Tibet: Evidence for
- 777 the consistent palaeolatitudes of the southern margin of Eurasia prior to the
- 778 collision with India. *Gondwana Research* 21, 53-63.
- 779 Tafti, R., Lang, J.R., Mortensen, J.K., Oliver, J.L., Rebagliati, C.M., 2014. Geology and
- 780 Geochronology of the Xietongmen (Xiongcu) Cu-Au Porphyry District,
- 781 Southern Tibet, China. *Economic Geology* 109, 1967-2001.
- 782 Tafti, R., Mortensen, J.K., Lang, J.R., Rebagliati, M., Oliver, J.L., 2009. Jurassic U-Pb
- 783 and Re-Os ages for the newly discovered xietongmen Cu-Au porphyry district,
- 784 tibet, PRC: Implications for metallogenic epochs in the Southern gangdese belt.
- 785 *Economic Geology* 104, 127-136.
- 786 Taylor, S.R., McLennan, S.M., 1985. The continental crust: its composition and
- 787 evolution. Blackwell's, Oxford.
- 788 Vermeesch, P., 2012. On the visualisation of detrital age distributions. *Chemical*
- 789 *Geology* 312-313, 190-194.
- 790 Wang, C., Ding, L., Zhang, L.Y., Kapp, P., Pullen, A., Yue, Y.H., 2016. Petrogenesis of
- 791 Middle–Late Triassic volcanic rocks from the Gangdese belt, southern Lhasa
- 792 terrane: Implications for early subduction of Neo-Tethyan oceanic lithosphere.
- 793 *Lithos* 262, 320-333.
- 794 Wang, C., Li, X., Liu, Z., Li, Y., Jansa, L., Dai, J., Wei, Y., 2012. Revision of the

- 795 Cretaceous–Paleogene stratigraphic framework, facies architecture and
796 provenance of the Xigaze forearc basin along the Yarlung Zangbo suture zone.
797 *Gondwana Research* 22, 415-433.
- 798 Wang, J.-G., Hu, X., Garzanti, E., An, W., Liu, X.-C., 2017a. The birth of the Xigaze
799 forearc basin in southern Tibet. *Earth and Planetary Science Letters* 465, 38-47.
- 800 Wang, J.-G., Hu, X., Garzanti, E., Ji, W.-Q., Liu, Z.-C., Liu, X.-C., Wu, F.-Y., 2017b.
801 Early Cretaceous topographic growth of the Lhasaplano, Tibetan Plateau:
802 Constraints from the Damxung Conglomerate: Topographic growth on Tibetan
803 Plateau. *Journal of Geophysical Research Solid Earth* 122.
- 804 Wei, Y., Zhao, Z., Niu, Y., Zhu, D.C., Dong, L., Wang, Q., Hou, Z., Mo, X., Wei, J.,
805 2017. Geochronology and geochemistry of the Early Jurassic Yeba Formation
806 volcanic rocks in southern Tibet: Initiation of back-arc rifting and crustal accretion
807 in the southern Lhasa Terrane. *Lithos* 278–281, 477-490.
- 808 Wronkiewicz, D.J., Condie, K.C., 1987. Geochemistry of Archean shales from the
809 Witwatersrand Supergroup, South Africa: Source-area weathering and provenance.
810 *Geochim. Cosmochim. Acta* 51, 2401-2416.
- 811 Wu, F.-Y., Ji, W.-Q., Liu, C.-Z., Chung, S.-L., 2010. Detrital zircon U–Pb and Hf
812 isotopic data from the Xigaze fore-arc basin: constraints on Transhimalayan
813 magmatic evolution in southern Tibet. *Chemical Geology* 271, 13-25.
- 814 Wu, F.-Y., Yang, Y.-H., Xie, L.-W., Yang, J.-H., Xu, P., 2006. Hf isotopic compositions
815 of the standard zircons and baddeleyites used in U–Pb geochronology. *Chemical*

- 816 Geology 234, 105-126.
- 817 Yan, D., Chen, D., Wang, Q., Wang, J., 2010. Large-scale climatic fluctuations in the
818 latest Ordovician on the Yangtze block, south China. *Geology* 38, 599-602.
- 819 Yin, A., Harrison, T.M., 2000. Geologic evolution of the Himalayan-Tibetan orogen.
820 *Annual Review of Earth and Planetary Sciences* 28, 211-280.
- 821 Zhang, K.J., Zhang, Y.X., Tang, X.C., Xia, B., 2012. Late Mesozoic tectonic evolution
822 and growth of the Tibetan plateau prior to the Indo-Asian collision. *Earth-Science*
823 *Reviews* 114, 236-249.
- 824 Zhang, Q., Ding, L., Cai, F., Xu, X.-X., Zhang, L., Xu, Q., Willems, H., 2011. Early
825 Cretaceous Gangdese retroarc foreland basin evolution in the Selin Co basin,
826 central Tibet: Evidence from sedimentology and detrital zircon geochronology.
827 *Geological Society, London, Special Publications* 353, 27-44.
- 828 Zhang, Z., Zhao, G., Santosh, M., Wang, J., Dong, X., Shen, K., 2010. Late Cretaceous
829 charnockite with adakititic affinities from the Gangdese batholith, southeastern
830 Tibet: Evidence for Neo-Tethyan mid-ocean ridge subduction? *Gondwana*
831 *Research* 17, 615-631.
- 832 Zhu, D.-C., Pan, G.-T., Chung, S.-L., Liao, Z.-L., Wang, L.-Q., Li, G.-M., 2008.
833 SHRIMP zircon age and geochemical constraints on the origin of Lower Jurassic
834 volcanic rocks from the Yeba Formation, southern Gangdese, South Tibet.
835 *International Geological Review* 50, 442-471.
- 836 Zhu, D.-C., Zhao, Z.-D., Niu, Y., Dilek, Y., Hou, Z.-Q., Mo, X.-X., 2013. The origin

- 837 and pre-Cenozoic evolution of the Tibetan Plateau. *Gondwana Research* 23,
838 1429-1454.
- 839 Zhu, D.-C., Zhao, Z.-D., Niu, Y., Mo, X.-X., Chung, S.-L., Hou, Z.-Q., Wang, L.-Q.,
840 Wu, F.-Y., 2011a. The Lhasa Terrane: Record of a microcontinent and its histories
841 of drift and growth. *Earth and Planetary Science Letters* 301, 241-255.
- 842 Zhu, D.C., Li, S.M., Cawood, P.A., Wang, Q., Zhao, Z.D., Liu, S.A., Wang, L.Q., 2016.
843 Assembly of the Lhasa and Qiangtang terranes in central Tibet by divergent
844 double subduction. *Lithos* 245, 7-17.
- 845 Zhu, D.C., Wang, Q., Cawood, P.A., Zhao, Z.D., Mo, X.X., 2017. Raising the Gangdese
846 Mountains in southern Tibet. *Journal of Geophysical Research: Solid Earth* 122.
- 847 Zhu, D.C., Zhao, Z.D., Niu, Y., Dilek, Y., Mo, X.X., 2011b. Lhasa terrane in southern
848 Tibet came from Australia. *Geology* 39, 727-730.
- 849

850 **Figure Captions**

851 **Fig. 1** (A) Schematic tectonic framework of the Tibetan Plateau (modified after Wu et
852 al., 2010) and (B) simplified geological map showing sample locations.

853

854 **Fig. 2** Outcrops show (A) mudstone interbedded with fine-grained sandstone in the
855 Chumulong Formation; (B) red beds of the Shexing Formation and (C) alternating
856 beds of sandstone and shale in the Ngamring Formation. Microphotographs show: (D)
857 the Chumulong Formation mudstone (D47D), (E) Shexing Formation sandstone
858 (MX1105) and (F) Ngamring Formation sandstone (RK1602). Q, quartz; Pl,
859 plagioclase; Kfs, potassic feldspar; Lv, volcanic lithic fragment; Ls, sedimentary lithic
860 fragment.

861

862 **Fig. 3** The Q-F-L ternary plot (Dickinson, 1985) showing clastic composition of
863 samples from the Yeba, Xiongkun, Chumulong and Shexing Formations. The
864 Xiongkun Formation data are from Lang et al., (2018). Q, quartz; F, feldspars; L,
865 lithic fragments; RO, recycled orogen; UMA, undissected magmatic arc; TMA,
866 transitional magmatic arc; DMA, dissected magmatic arc; BU, basement uplift; TC,
867 transitional continental; CI, craton interior.

868

869 **Fig. 4** Kernel density estimation plots of detrital zircon U-Pb ages for clastic rocks

870 from the Yeba (A and B), Chumulong (C and D) and Shexing (E and F) Formations

871

872 **Fig. 5** Hf isotope composition of detrital zircons from the Chumulong and Shexing
873 Formations. The field of GMA and Lhasa basement are constructed based on the
874 dataset in Hou et al., (2015) and references therein. Data of the Duoni Formation from
875 Sun et al., (2017). GMA, Gangdese magmatic arc; DM, depleted mantle; CHUR,
876 chondritic uniform reservoir.

877

878 **Fig. 6** (A-F) Plot of SiO_2 vs. abundances of major element oxide for the sandstone
879 and mudstone samples; (G-L) plots of modal volcanic lithics proportion vs.
880 concentrations or ratios of selected elements for the sandstone samples.

881

882 **Fig. 7** (A-D) Chondrite-normalized REE and (E) UCC-normalized multielement
883 diagrams for the sediments in the southern Lhasa terrane. Chondrite and UCC (upper
884 continental crust) data from Sun and McDonough (1989) and Rudnick and Gao
885 (2003), respectively. Unweathered Yeba volcanics data from Wei et al. (2017).

886

887 **Fig. 8** Ternary plots of (A) A-CN-K and (B) A-CNK-FM showing sandstones and
888 mudstones from the Jurassic-Cretaceous strata in the southern Lhasa terrane (after
889 Nesbitt and Young, 1989; McLennan et al., 1993). The Xiongkun Formation data are
890 from Lang et al., (2018). A = Al_2O_3 , C = CaO^* , N = Na_2O , K = K_2O , F = total Fe as

891 FeO, $M = MgO$.

892

893 **Fig. 9** Plot of Th vs. Th/U for the clastic rocks from the southern Lhasa terrane (after
894 McLennan et al., 1993). Yeba Formation volcanic rock data from Wei et al. (2017)
895 and Zhu et al. (2008).

896

897 **Fig. 10** Ternary plots of Th-Sc-Zr/10 and La-Th-Sc for the sediments from the
898 southern Lhasa terrane, where GMA = Gangdese magmatic arc, ACM = active
899 continental margin, PCM = passive continental margin, CA = continental arcs, OA =
900 oceanic arcs (After Bhatia and Crook, 1986). GMA Array is defined using data of the
901 Yeba volcanic rocks (Wei et al., 2017).

902

903 **Fig. 11** Binary diagram of La/Sc-Co/Th showing two-component mixing trend. Mafic
904 endmember is represented by the Yeba Formation basalt (sample YB1307 in Wei et al.,
905 2017) with Co=39.3ppm, Th=1.18ppm, La=10.9ppm and Sc=33.8ppm. Silicic
906 endmember is represented by the Yeba Formation rhyolite (sample YB1318 in Wei et
907 al., 2017) with Co=3.1ppm, Th=8.89ppm, La=27.3ppm and Sc=6.4ppm.

908

909 **Fig. 12** Stratigraphic columns showing compositional variations of the sediments and
910 detrital zircon sample location in different lithostratigraphic units. Columns after An
911 et al. (2014); Leier et al. (2007a); Leier et al. (2007b); Wang et al. (2012); Zhu et al.

912 (2013). CIA serves as an indicator of chemical weathering intensity. Eu/Eu^* reflects
913 enrichment of volcanic lithics. $\text{Na}_2\text{O}/\text{K}_2\text{O}$ measures compositional maturity.
914 Thicknesses of different units are not to scale. Timescale in Ma from Cohen et al.
915 (2013). The average composition of upper continental crust ($\text{Eu}/\text{Eu}^*=0.65$,
916 $\text{Na}_2\text{O}/\text{K}_2\text{O}=1.2$) are introduced for reference.

917

918 **Fig.13** Summary of detrital zircon age spectra of sedimentary rocks of this study and
919 previous work. Important age peaks are shown in colored bands. The red line
920 represents kernel density estimation. Data of the (A) western Australia, (B)
921 Permo-Carboniferous Lhasa and (G) western Qiangtang from Zhu et al., 2011b and
922 references therein; (C) Late Triassic Lhasa from Cai et al. (2016); (D) Early Jurassic
923 Lhasa from this study; (E) Early Cretaceous Lhasa from Leier et al. (2007c) and this
924 study; (F) Late Cretaceous Lhasa from Kapp et al. (2007), Leier et al. (2007c), Pullen
925 et al. (2008) and this study.

926

927 **Fig. 14** Schematic illustrations showing tectonic evolution of the Lhasa terrane during
928 the Jurassic-Cretaceous time (not to scale). See text for details.

929

930 **Table Caption**

931 **Table 1** Summarized characteristics of detrital zircon U-Pb ages for clastic samples

932 from the southern Lhasa terrane

Journal Pre-proof

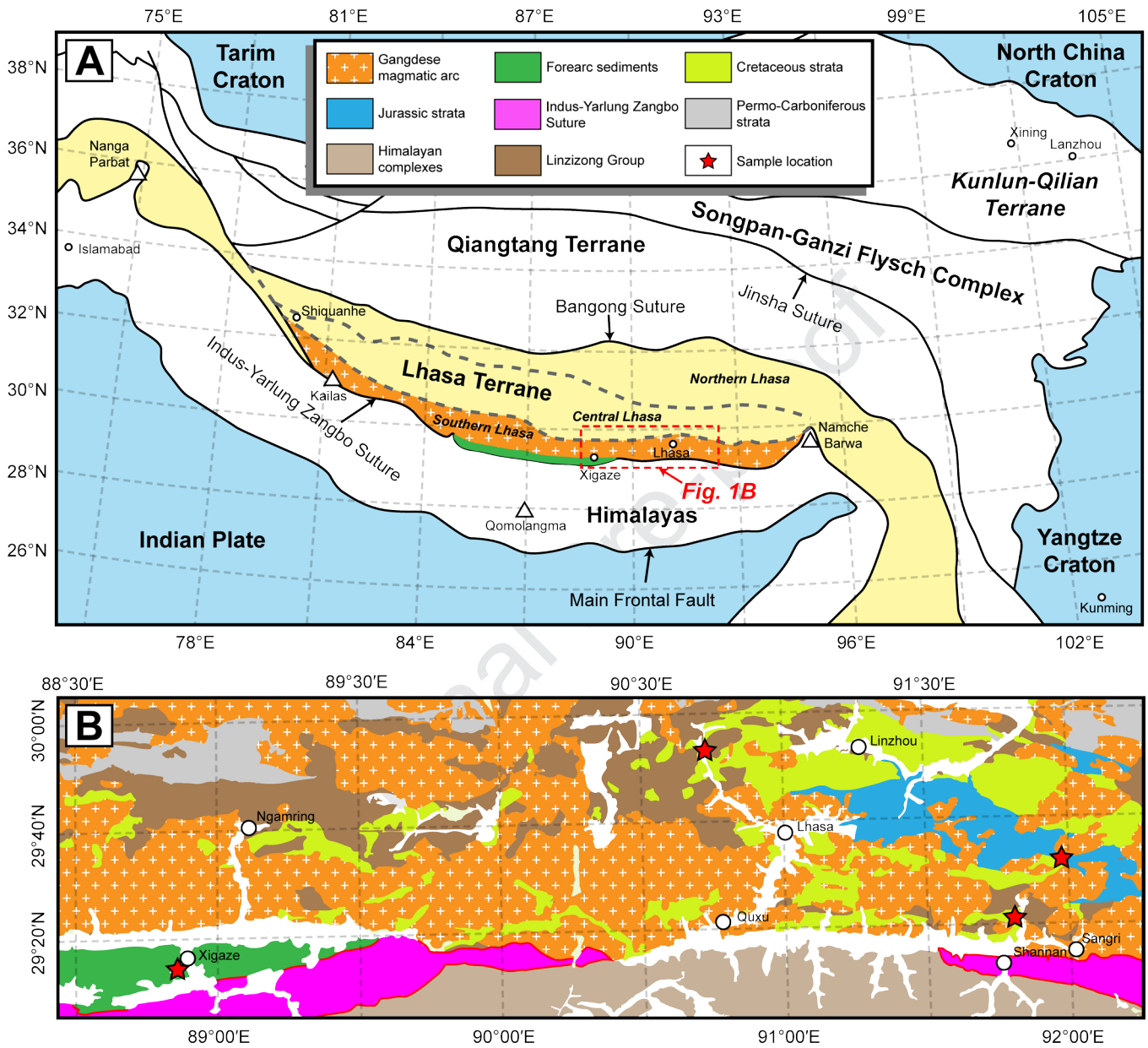
Table 1 Summarized characteristics of detrital zircon U-Pb ages for samples from southern Lhasa terrane

Formation	Sample	Number of analyses	Maximum depositional age (Ma)	YSG ^a (Ma, 1 σ)	YC1 σ (2+) ^a (Ma)	YC2 σ (3+) ^a (Ma)	Percentage of Mesozoic ages	Mesozoic zircons with $\epsilon\text{Hf}(t)>0$
Yeba	D54	104	179 ^b	179 \pm 2	563.5 \pm 3.6 (n=6)	248.0 \pm 3.5 (n=3)	4.8% (5 out of 104)	
	D47A	103	121	117 \pm 1	121.1 \pm 1.1 (n=4)	121.1 \pm 1.1 (n=4)	24% (25 out of 103)	
Chumulong	D47B	109	122	105 \pm 1	122.4 \pm 1.3 (n=4)	123.3 \pm 0.9 (n=7)	34% (37 out of 109)	41% (18 out of 44)
	D47C	68	119 ^b	119 \pm 2	394.0 \pm 4.2 (n=4)	401.4 \pm 2.2 (n=11)	1.4% (1 out of 68)	
	D47E	47	109 ^b	109 \pm 1	231.5 \pm 2.8 (n=2)	247.9 \pm 2.6 (n=3)	32% (15 out of 47)	
Shexing	MX1102	113	88	84 \pm 2	88.5 \pm 1.4 (n=2)	88.8 \pm 1.3 (n=3)	25% (28 out of 113)	
	MX1104	90	90	85 \pm 1	89.9 \pm 0.7 (n=15)	89.7 \pm 0.6 (n=18)	52% (47 out of 90)	67% (70 out of 104)
	MX1106	86	88	82 \pm 2	87.7 \pm 0.5 (n=30)	87.1 \pm 0.5 (n=35)	83% (71 out of 86)	
	MX1108	88	91 ^b	91 \pm 2	213.3 \pm 3.5 (n=3)	213.3 \pm 3.5 (n=3)	6.8% (6 out of 88)	

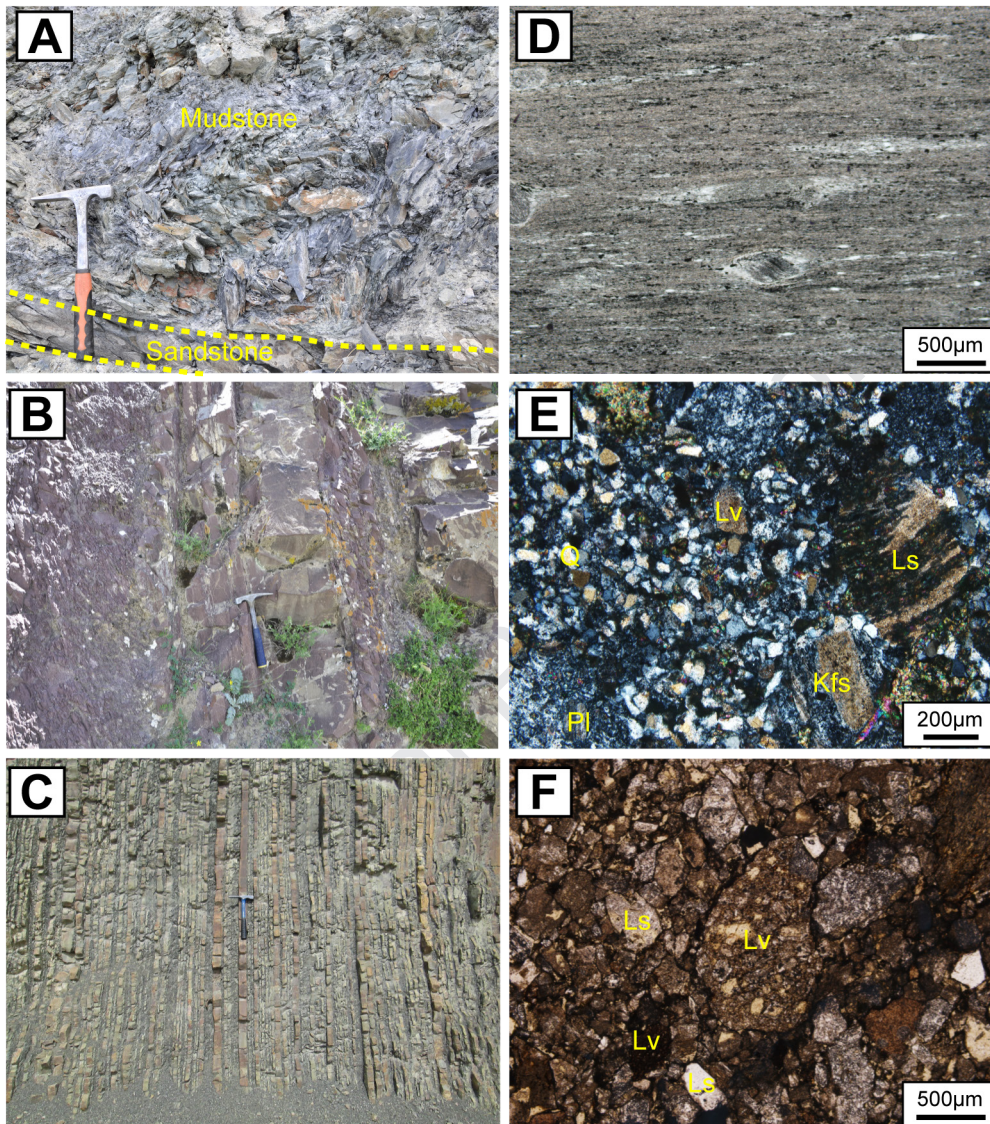
^a Youngest detrital zircon age measurement after Dickinson and Gehrels (2009). YSG, youngest single detrital zircon age; YC1 σ (2+), weighted mean age of two or more youngest grains that overlap in age at 1 σ ; YC2 σ (3+), weighted mean age of three or more youngest grains that overlap in age at 2 σ .

^b YSG is suggested due to the inconsistency of YC2 σ with the depositional ages determined via other samples/methods.

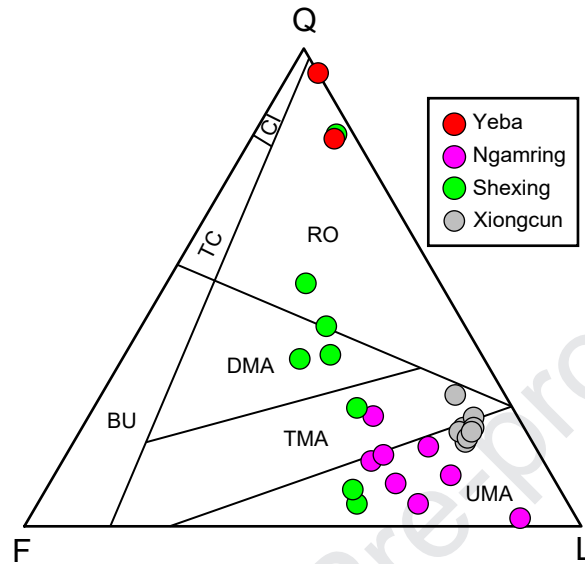
Wei et al. Fig.1 W179mm - H163mm (2-column fitting image)



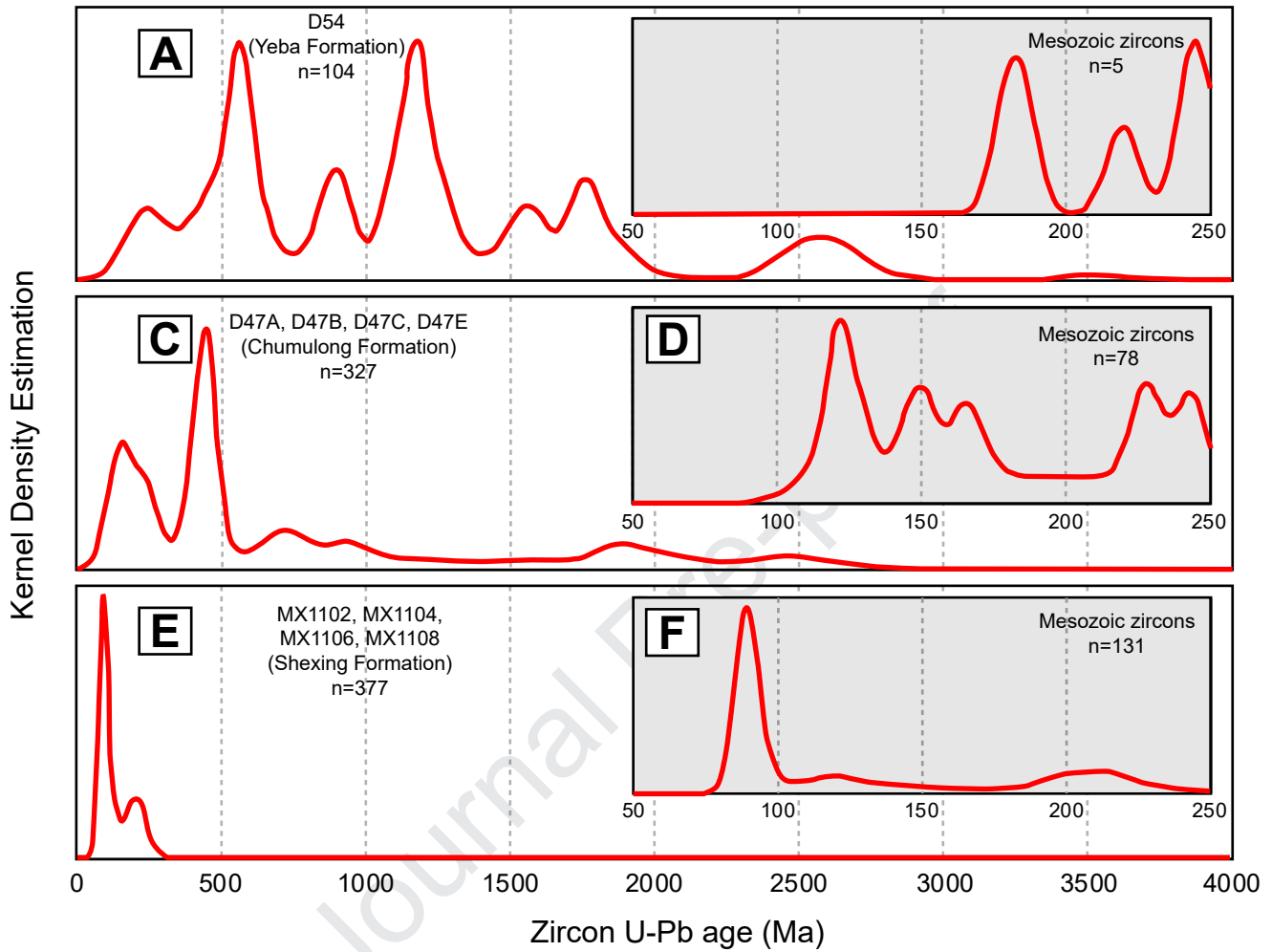
Wei et al. **Fig.2** W132mm - H149mm (2-column fitting image)



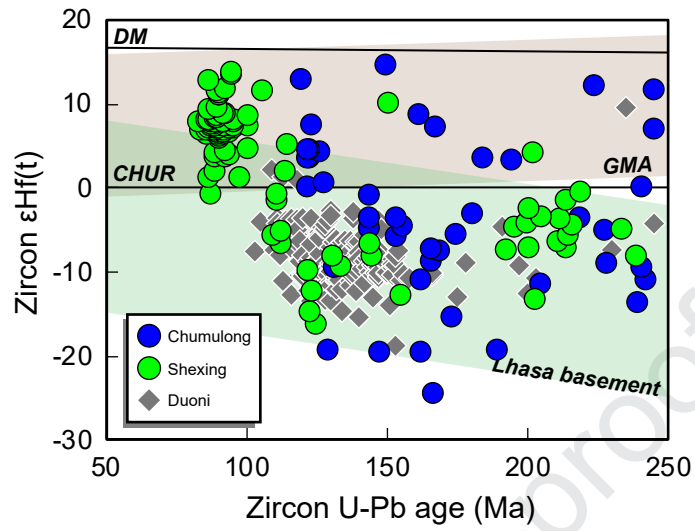
Wei et al. Fig.3 W77mm - H75mm (1-column fitting image)



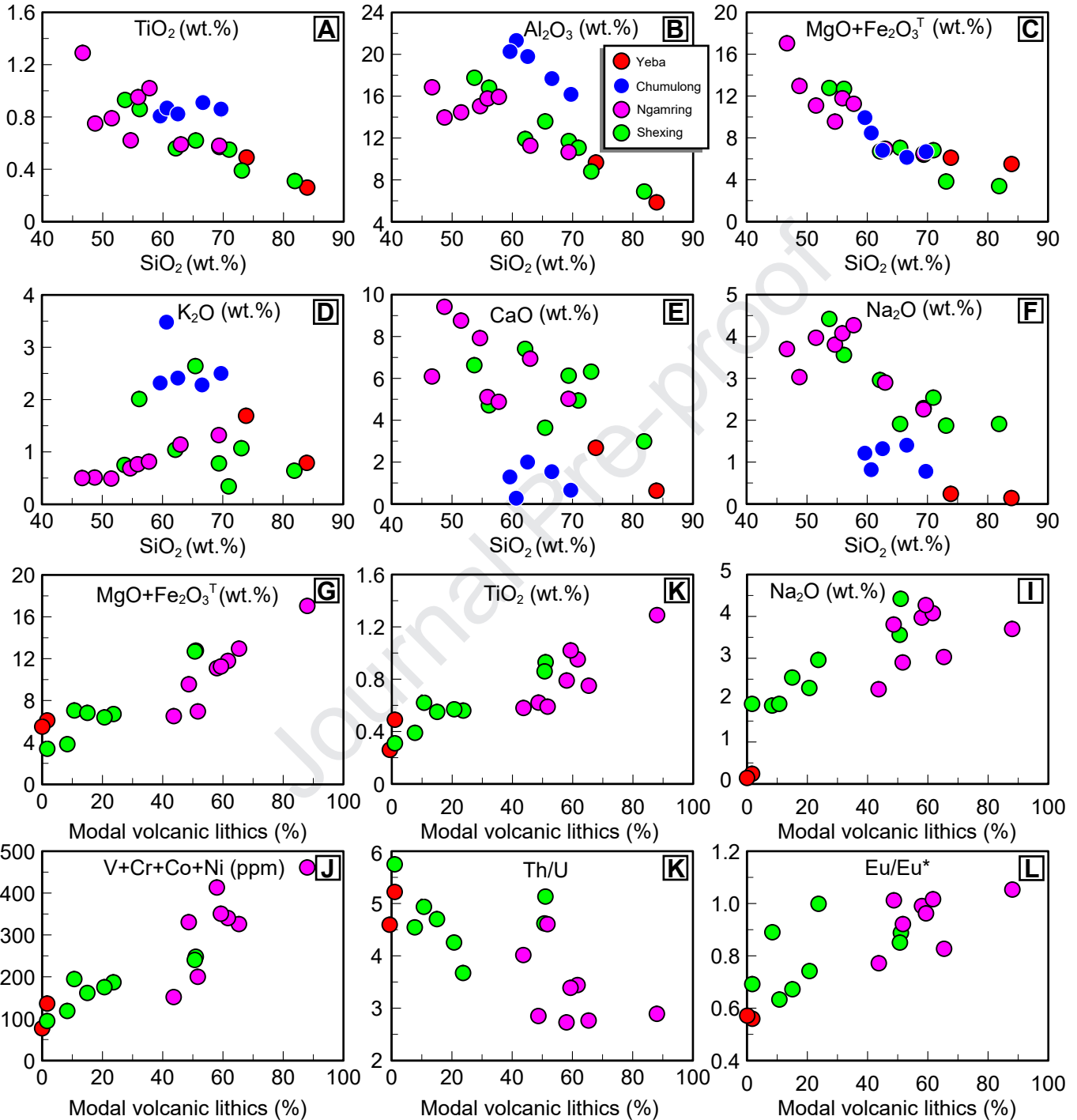
Wei et al. Fig.4 W174mm - H151mm (2-column fitting image)



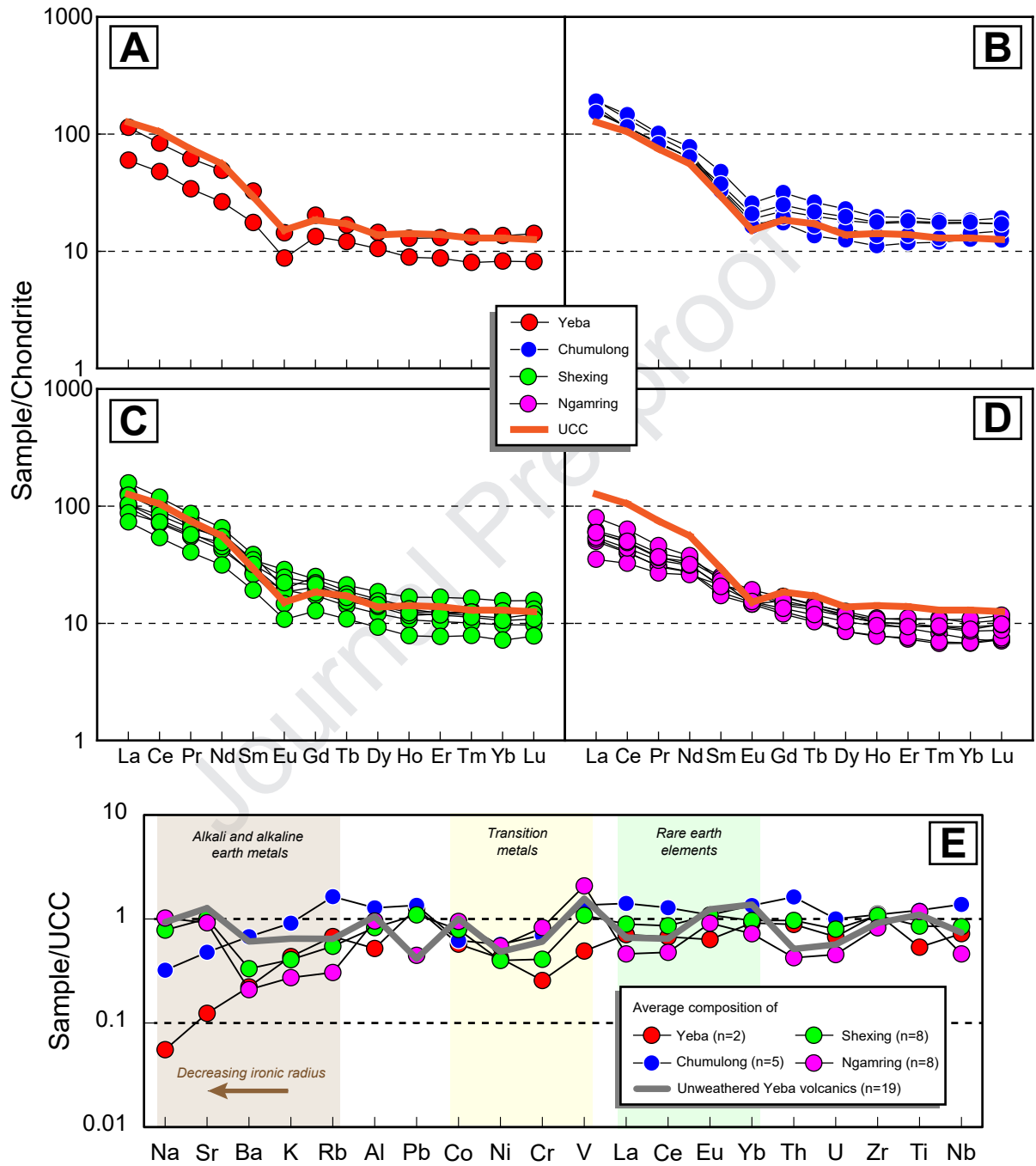
Wei et al. **Fig.5** W90mm - H69mm (1-column fitting image)



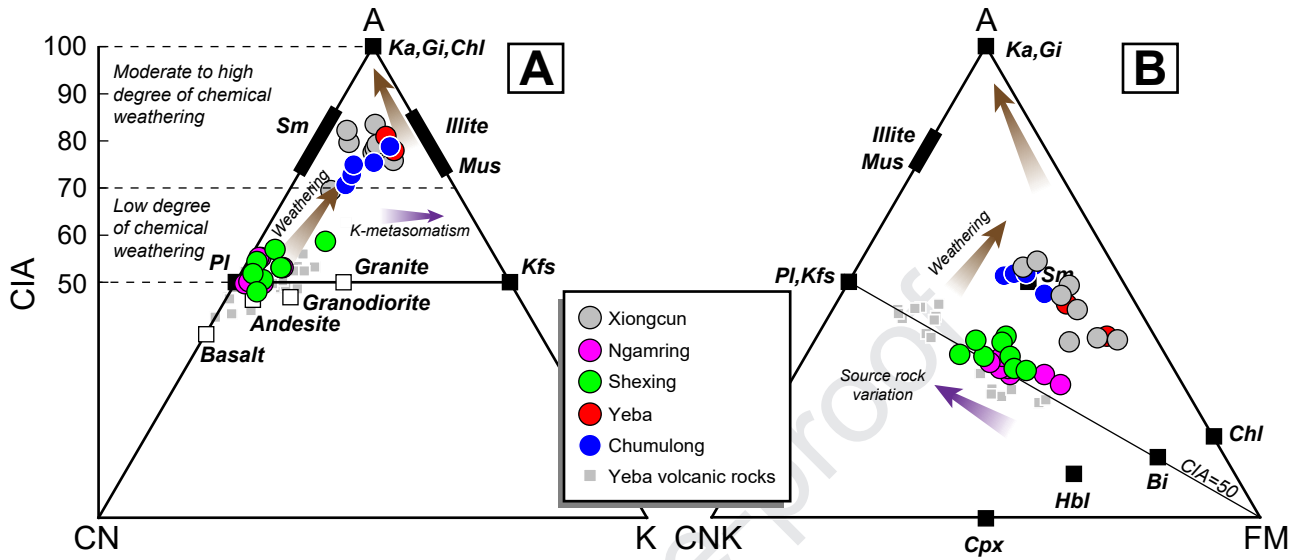
Wei et al. Fig.6 W179mm - H188mm (2-column fitting image)



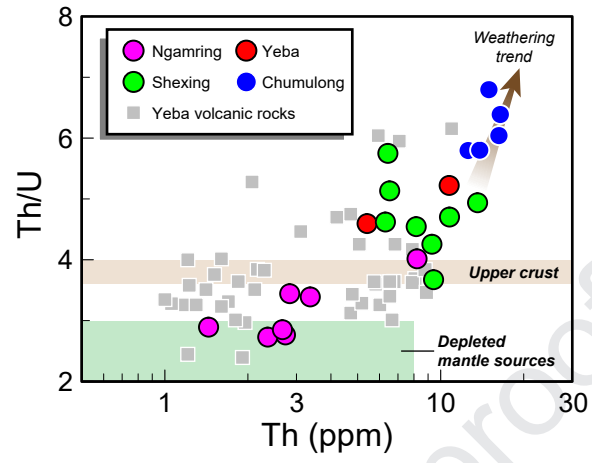
Wei et al. Fig.7 W158mm - H179mm (2-column fitting image)

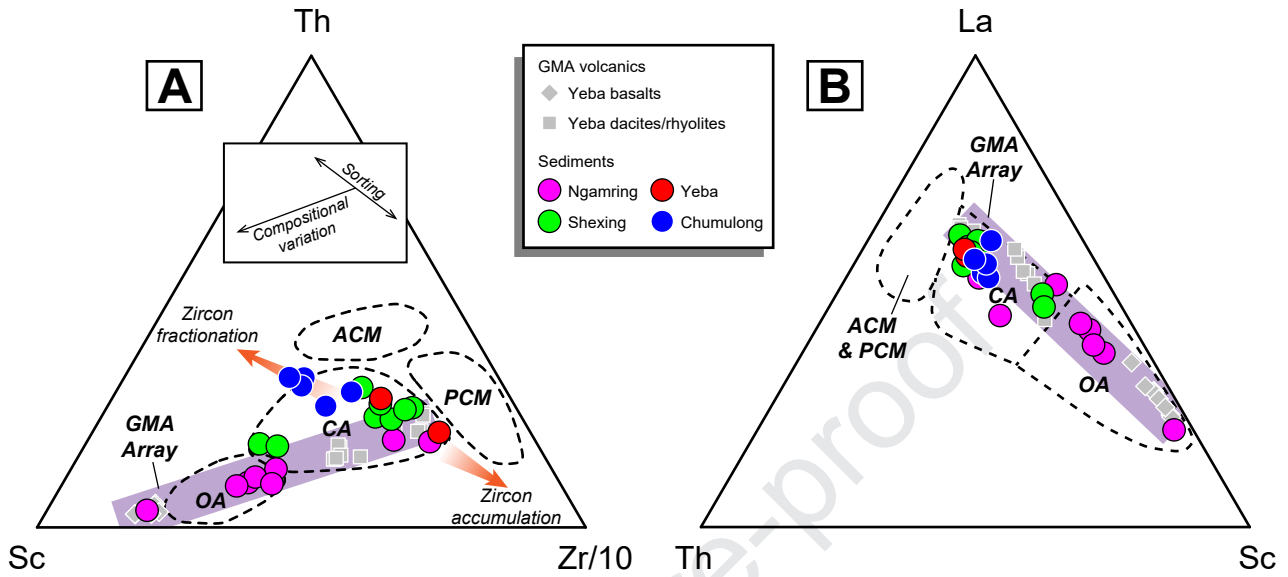


Wei et al. Fig.8 W170mm - H74mm (2-column fitting image)

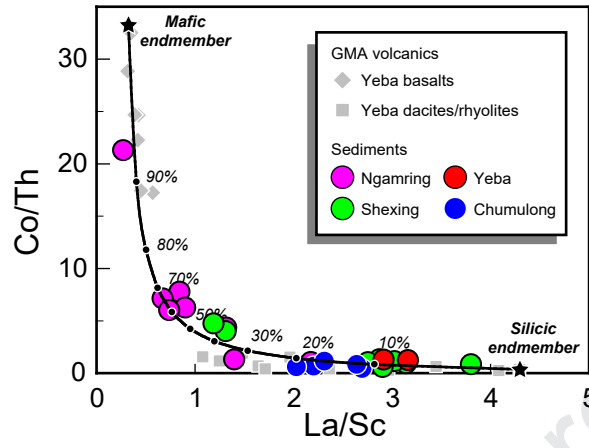


Wei et al. **Fig.9** W77mm - H60mm (1-column fitting image)

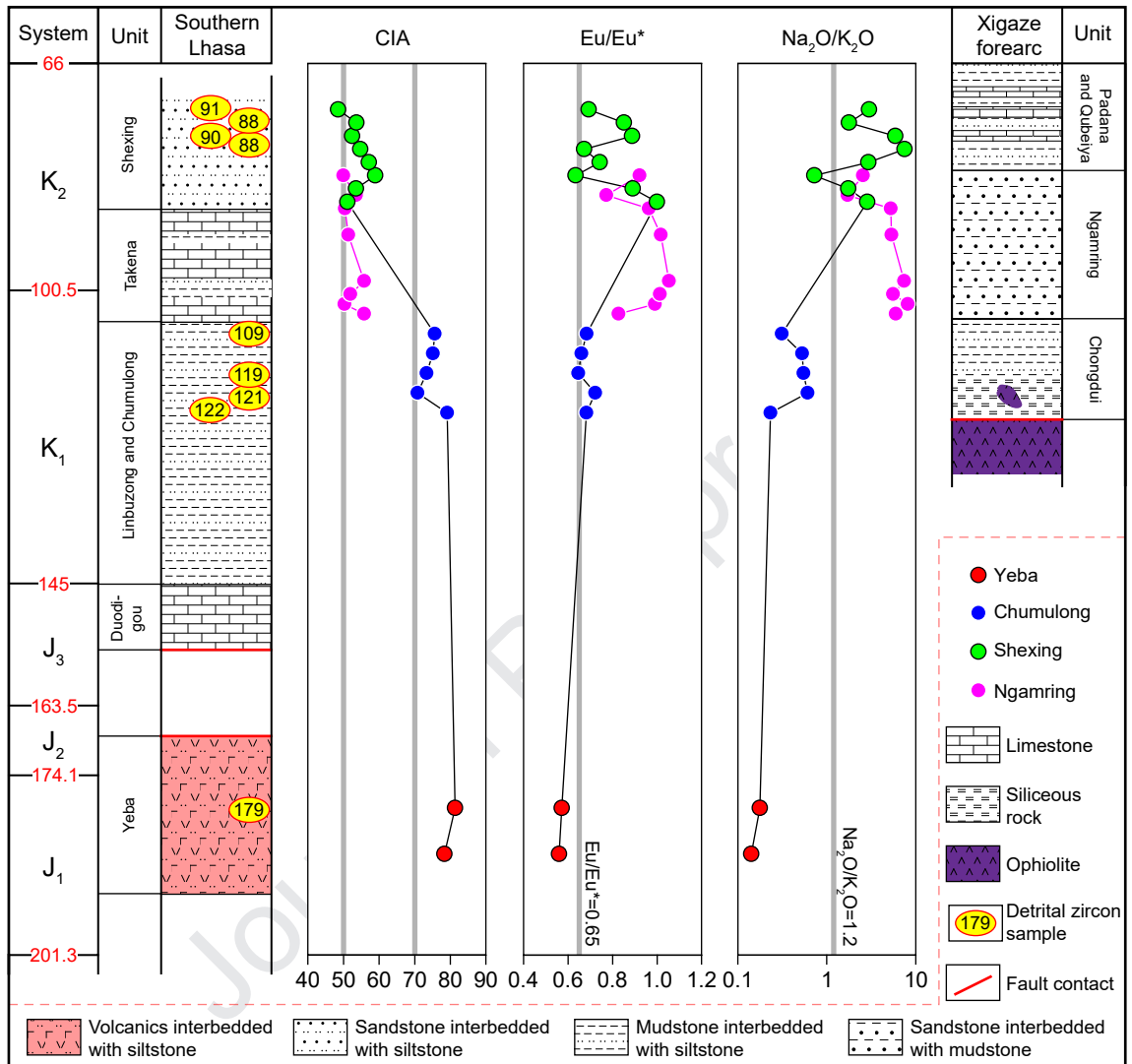


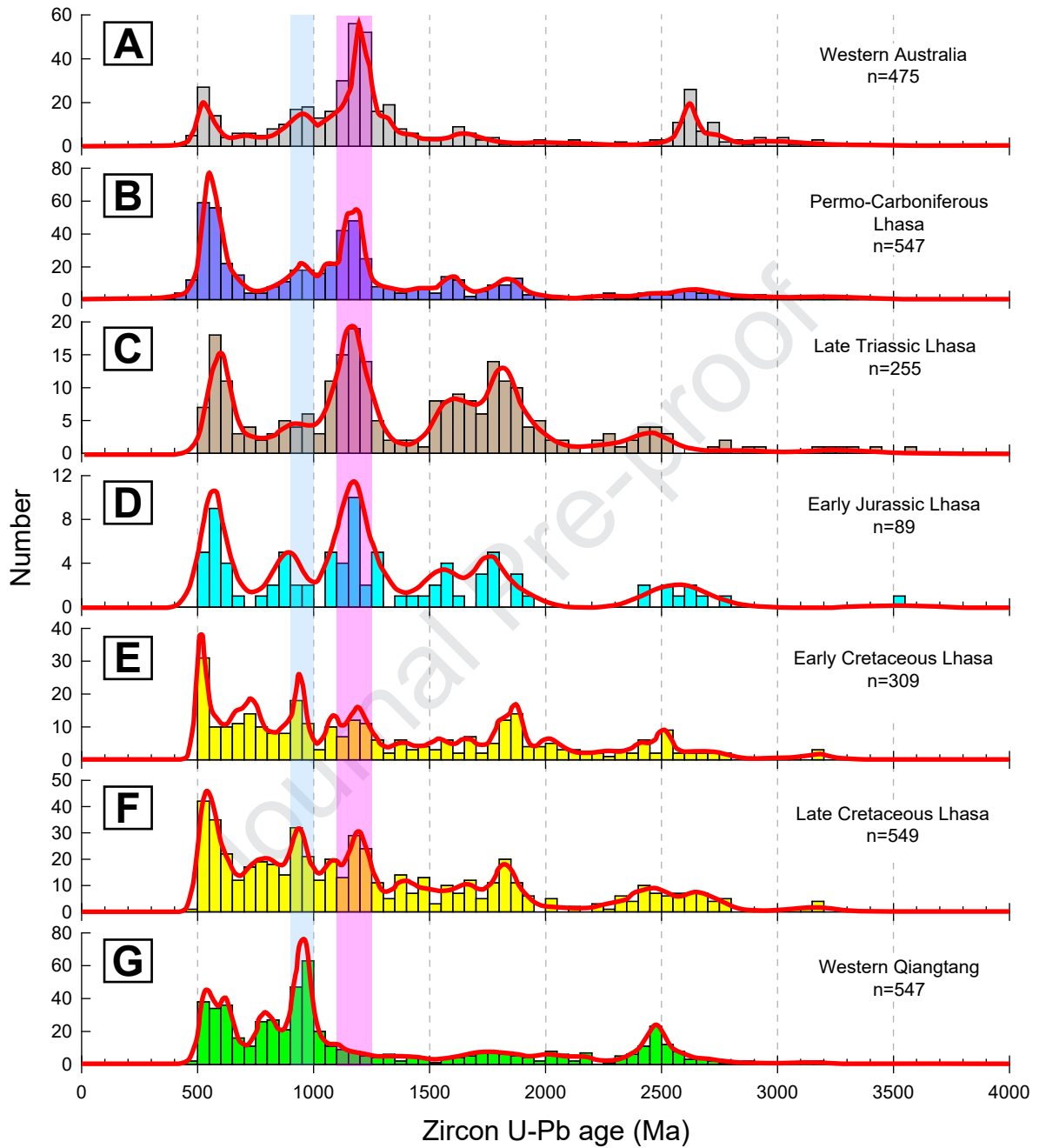
Wei et al. **Fig.10** W168mm - H76mm (2-column fitting image)

Wei et al. **Fig.11** W78mm - H59mm (1-column fitting image)

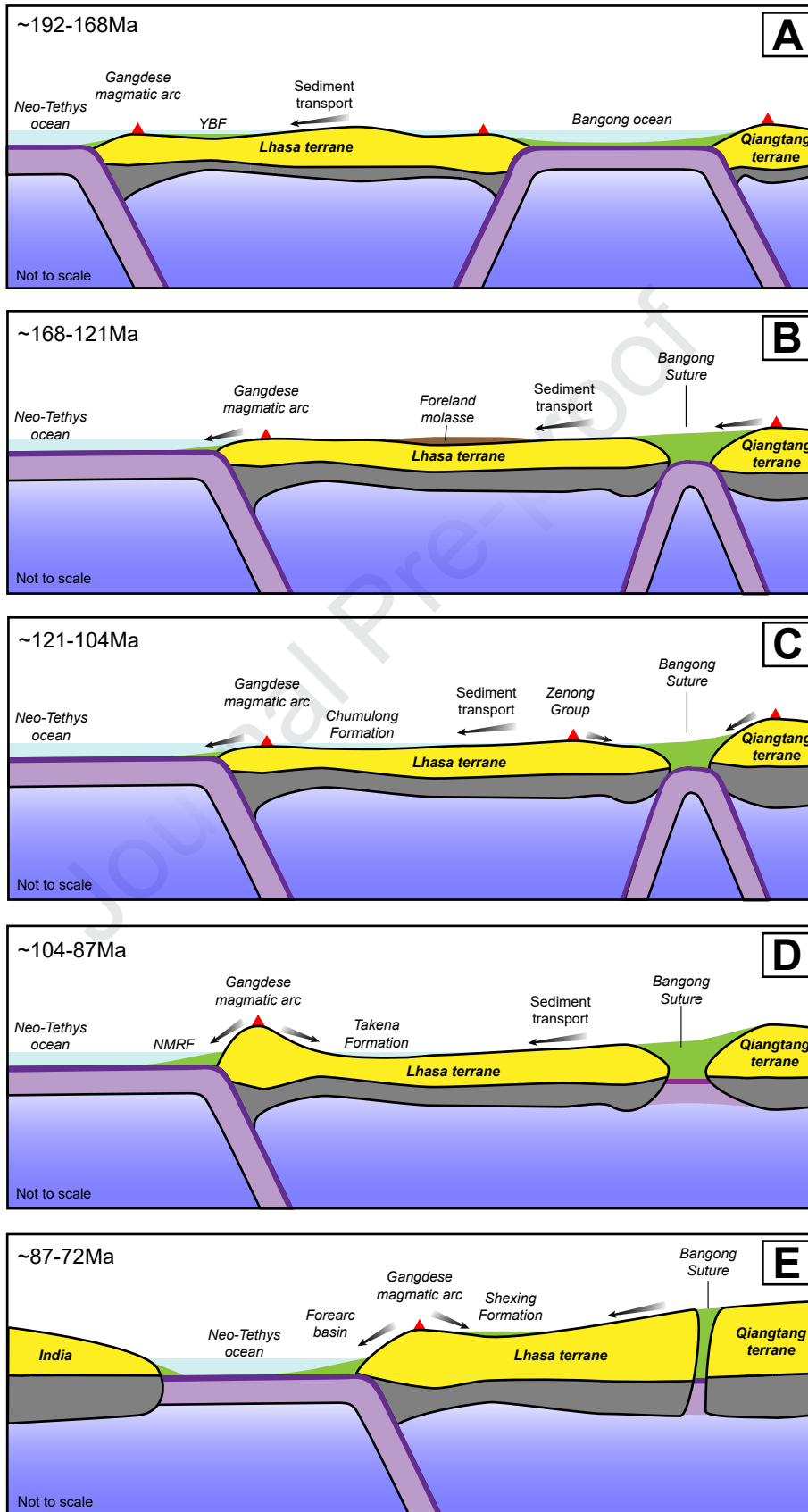


Wei et al. Fig.12 W150mm - H143mm (2-column fitting image)



Wei et al. Fig.13 W156mm - H174mm (2-column fitting image)

Wei et al. Fig.14 W121mm - H223mm (2-column fitting image)



Highlights

- Jurassic-Cretaceous tectonic evolution of the Lhasa terrane was reconstructed.
- Maximum depositional ages of strata in the southern Lhasa terrane were constrained.
- Sedimentary processes were quantified using sedimentary geochemistry approach.
- Two-component mixing model was constructed to evaluate the sedimentary provenances.
- The Lhasa terrane received clasts from Qiangtang since the Early Cretaceous.